Uranium metallogenesis of the peraluminous leucogranite from the Pontivy-Rostrenen magmatic complex (French Armorican Variscan belt): the result of long-term oxidized hydrothermal alteration during strike-slip deformation

Christophe Ballouard, Marc Poujol, Julien Mercadier, Etienne Deloule, Philippe Boulvais, Michel Cuney, Michel Cathelineau, Jean-Marc Baele

Uranium metallogenesis of the peraluminous leucogranite from the Pontivy-Rostrenen magmatic complex (French Armorican Variscan belt): the result of long term oxidized hydrothermal alteration during strike-slip deformation.

Ballouard C.[a, b]*, Poujol M.[a], Mercadier J. [c], Deloule E.[c], Boulvais P.[a], Baele J.M.[e], Cuney M.[c], Cathelineau M.[c]

[a] UMR CNRS 6118, Géosciences Rennes, OSUR, Université Rennes 1, 35042 Rennes Cedex, France

[b] Department of Geology, University of Johannesburg, PO Box 254, Auckland Park 2006, South Africa

[c] Université de Lorraine, CNRS, CREGU, GeoRessources, Boulevard des Aiguillettes, BP 70239, 54506 Vandoeuvre-lès-Nancy, France

[d] CRPG, UMR 7358 CNRS-Université de Lorraine, BP20, 54501 Vandoeuvre Cedex, France

[e] Department of Geology and Applied Geology, University of Mons, 20 Place du Parc, Mons 7000, Belgium

Keywords: Uranium deposits, syntectonic granites, apatite geochemistry and U-Pb dating, fluid-rock interactions, Hercynian, south Armorican shear zone

Abstract

In the French Armorican Variscan belt, most of the economically significant hydrothermal U deposits are spatially associated with peraluminous leucogranites emplaced along the south Armorican shear zone (SASZ), a dextral lithospheric scale wrench fault that recorded ductile deformation from ca. 315 to 300 Ma. In the Pontivy-Rostrenen complex, a composite intrusion, the U mineralization is spatially associated with brittle structures related to deformation along the SASZ. In contrast to monzogranite and quartz monzodiorite ($3 < U < 9$ ppm; $Th/U > 3$), the

leucogranite samples are characterized by highly variable U contents (~3 to 27 ppm) and Th/U ratios (~0.1 to 5) suggesting that the crystallization of magmatic uranium oxide in the more evolved facies was followed by uranium oxide leaching during hydrothermal alteration and/or surface weathering. U-Pb dating of uranium oxides from the deposits reveals that they mostly formed between ca. 300 and 270 Ma. In monzogranite and quartz monzodiorite, apatite grains display magmatic textures and provide U-Pb ages of ca. 315 Ma reflecting the time of emplacement of the intrusions. In contrast, apatite grains from the leucogranite display textural, geochemical and geochronological evidences for interaction with U-rich oxidized hydrothermal fluids contemporaneously with U mineralizing events. From 300 to 270 Ma, infiltration of surface-derived oxidized fluids leached magmatic uranium oxide from fertile leucogranite and formed U deposits. This phenomenon was sustained by brittle deformation and by the persistence of thermal anomalies associated with U-rich granitic bodies.

Introduction

Continental scale wrench faults represent common tectonic features in orogenic belts, which act as channels for crustal and mantle derived magmas (Strong and Hanmer 1981; D'Lemos et al. 1992; Hutton and Reavy 1992; De Saint Blanquat et al. 1998; Brown 2010; Pirajno, 2010) as well as hydrothermal fluids (e.g. Sibson 1987, 1990; Faulkner et al. 2010; López-Moro et al. 2013; Cao and Neubauer 2016). Major strike-slip faults initiate deep within the crust and the lithospheric mantle due to rheological weakening (Cao and Neubauer 2016). During the exhumation of these tectonic systems, a thermal evolution occurs: brittle deformation (cataclasites, pseudotachylytes) is superimposed on ductile deformation (mylonites) and the ascent of magmas as well as hot lower crustal, and magmatic derived fluids is followed by the downward flow of cold surface-derived water. Therefore, these strike-slip deformation zones can represent an important metallotect for hydrothermal uranium (U) deposits if they affect U fertile lithologies. Among U-rich igneous rocks, felsic volcanic rocks and peraluminous

leucogranite represent an ideal source for the formation of hydrothermal U deposits because most of their U is hosted in easily leachable glass and uranium oxide, respectively (Cuney 2014). The relationships between U-rich felsic volcanic rocks, strike-slip faults, and hydrothermal uranium deposits are for example well illustrated in South China, along the southern termination of the Tan Lu fault (Li et al. 2001, 2002). Similarly, the association between peraluminous leucogranite, wrench faults and U mineralization exists, for example, in Egypt along the El Sela shear zone (Gaafar et al. 2014; Gaafar 2015) and in the European Variscan belt (EVB): the Alentejo-Plasencia strike-slip fault in Iberia (Pérez Del Villar and Moro 1991) and the north-western part of the Massif Central (France; Cathelineau et al. 1990; Cuney et al. 1990; Gébelin et al. 2009) (Fig. 1).

The Armorican Massif (France) in the EVB (Figs. 1 and 2) represents a historical mining province for U where about 20 000 t U (~20 % of the French production; IRSN 2004) have been extracted before the end of the 90's. Few minor deposits are associated with Late Carboniferous metaluminous granitoids emplaced along the north Armorican shear zone (NASZ; Chauris 1984), a crustal-scale, dextral, strike slip fault with a limited displacement of ~20 km (Fig. 2) (Jégouzo 1980). The majority of the U deposits are spatially associated with Late Carboniferous peraluminous syntectonic leucogranite emplaced either along extensional deformation zones (Guérande leucogranite; Cathelineau 1981; Ballouard et al. 2017a) or along the south Armorican shear zone (SASZ: Mortagne and Pontivy leucogranites; Cathelineau 1982; Cathelineau et al. 1990; Cuney et al. 1990), a lithospheric-scale, dextral wrench fault with a displacement of ~200 km (Fig. 2) (Berthé et al. 1979; Gapais and Le Corre 1980; Jégouzo 1980, Jégouzo and Rosselo 1988; Judenherc et al. 2003; Gumiaux et al. 2004a, 2004b; Tartèse et al. 2012). Recent studies on mylonite, leucogranite and quartz veins along the SASZ demonstrated that, during Late Variscan times, this fault acted as a major channel for lower crustal but also meteoric-derived oxidized hydrothermal fluids (Tartèse and Boulvais 2010;

Tartèse et al. 2012; Lemarchand et al. 2012). These fluids were able to transport an important quantity of uranium in solution (Dubessy et al. 1987).

The Pontivy-Rostrenen syntectonic composite intrusion hosts U intragranitic deposits associated with peraluminous leucogranite (Figs. 2 and 3). U was interpreted to originate from leaching of uranium oxides from the surrounding leucogranite (Marcoux 1982), although the metallogenic model remains poorly constrained. In this study, we use geochemical analyses and U-Pb dating of apatite from the granitoids as well as U-Pb dating of uranium oxides from the deposits to determine the timing and conditions of hydrothermal U mobilization and then its precipitation in the deposits. We then discuss this model in the geodynamic and metallogenic frameworks at the scale of the region and the EVB.

Geological framework

The Armorican Massif as part of the European Variscan belt

The Armorican Massif belongs to the EVB, a Paleozoic orogenic belt which extends throughout the western (Iberian Massif) and central Europe (Bohemian Massif) and results from the collision of supercontinents Laurussia and Gondwana (Ballèvre et al. 2009, 2013, 2014; Kroner and Romer 2013) (Fig.1). The structure of the EVB is a consequence of a complex interaction between low-strain and high-strain domains (Kroner and Romer 2013). Low strain domains, such as Ibero-Armorica, represent blocks of thick continental crust drifted from the northern Gondwana margin during Cambrian-Ordovician extension whereas high strain domains, such as the Massif Central and southern part of the Armorican Massif, that were highly deformed during Variscan orogeny, represent domains of Gondwana crust thinned during Lower Paleozoic extension (Kroner and Romer, 2013). Continental subduction events in the Variscides occurred until ca. 350-340 Ma and transition from a compressive to an extensive regime occurred ca. 315-300 Ma ago (Kroner and Romer, 2013; Ballèvre et al. 2014).

98 The Armorican Massif is separated into three main domains by the NASZ and the SASZ
99 (Fig. 2). The northern domain is mostly made of a Proterozoic basement (e.g. Brun et al. 2001),
100 locally intruded by Variscan granitoids. The central domain is composed of Late Proterozoic
101 (Brioverian) to Lower Carboniferous sedimentary rocks mostly deformed under greenschist
102 facies conditions during dextral wrenching along the NASZ and SASZ in Carboniferous times
103 (Gumiaux et al. 2004a). The deformation in this area is marked by a vertical foliation associated
104 with a sub-horizontal stretching lineation (Jégouzo 1980). The southern domain, which belongs
105 to the internal part of the Variscan belt, is characterized by a higher degree of deformation and
106 by the presence of high grade metamorphic rocks (Gapais et al. 2015). Three tectono-
107 metamorphic units can be distinguished in this domain and include, from top to bottom, HP-LT
108 rocks, composed of blueschists and metavolcanic rocks subducted and exhumed during early
109 tectonic events from 370 to 350 Ma (Bosse et al. 2005), micaschists, and migmatite bearing
110 units (Fig. 2). Between 315 and 300 Ma (Tartèse et al. 2012), the SASZ acted as a transfer zone
111 between the southern domain, where crustal extension lead to the exhumation of core
112 complexes cored by migmatites and synkinematic leucogranites, and the central domain
113 deformed by pervasive dextral wrenching (Gapais et al. 2015).

114 During the Late Carboniferous, the Armorican Massif was intruded by various granitoids
115 ranging from peraluminous to metaluminous in composition (Capdevilla 2010; Fig. 2). To the
116 south, two mica peraluminous leucogranites are characteristic. They were emplaced either
117 along extensional deformation zone in the southern domain, such as the Quiberon (Gapais et al.
118 1993, 2015), Sarzeau (Turrillot et al. 2009) and Guérande (309.7 ± 1.3 Ma: leucogranites, or
119 along, the SASZ such as the Lizio (316.4 ± 5.6 Ma: Tartèse et al. 2011a), Questembert (316.1
120 ± 2.9 Ma : Tartèse et al. 2011b) and Pontivy (316.7 ± 2.5 Ma: Ballouard et al. 2017b)
121 leucogranites. To the north, a bimodal magmatism occurred as expressed by the emplacement
122 of Bt ± cordierite (Cd) peraluminous granites, associated with intermediate rocks of mantle

123 origin, such as the Rostrenen (315.5 ± 2.0 Ma: Ballouard et al. 2017b) and Huelgoat intrusions
124 (314.8 ± 2.0 Ma: Ballouard 2016) and two suites of biotite ± hornblende metaluminous
125 granitoids. These granitoids consist of a magneso-potassic and a ferro-potassic suite emplaced
126 between 320 and 300 Ma and associated with mantle-derived mafic to intermediate rocks
127 (Ballouard et al. 2017b). On a regional scale, the crustal magmatism to the south of the SASZ
128 was triggered by late-orogenic crustal extension. In contrast, to the north, partial melting of the
129 crust and mantle, enriched during earlier subduction events, were triggered by an asthenosphere
130 upwelling during strike-slip deformation and subsequent slab-tearing (Ballouard et al. 2017b).

131 The EVB represents an important metallogenic province for U where vein, episyenite-type,
132 breccia-hosted or shear zone-hosted U deposits occur all over the belt. Major occurrences are
133 located in the Iberian Massif, the Armorican Massif, the Massif Central and the Bohemian
134 Massif (Fig. 1). A large proportion of these hydrothermal U deposits are spatially associated
135 with Late Carboniferous low Ca peraluminous two mica (or biotite) granite (Fig. 1) and main
136 U mineralizing events in the EVB occurred during the Permian from 300 to 260 Ma (Cuney et
137 al. 1990; Cathelineau et al 1990; Tischendorf and Förster 1994; Cuney and Kyser, 2008; Romer
138 et al. 2010; Ballouard et al. 2017a).

139 In the Armorican Massif, U has been mostly mined in the Guérande, Pontivy and Mortagne
140 districts (Fig. 2). In the Guérande district, the most important vein deposit (Pen Ar Ran) is
141 perigranitic and localized above the apical zone of the Guérande leucogranite (Cathelineau
142 1981). The Guérande leucogranite itself was the main source for U (Ballouard et al. 2017a).
143 Trace elements and oxygen isotope compositions suggest that hydrothermal leaching of the
144 magmatic uranium oxides in deformed facies of the apical zone was promoted by the infiltration
145 of surface-derived oxidized fluids. The leached U was then precipitated in the reducing
146 environment represented by black shales and graphitic quartzites (Ballouard et al. 2017a). The
147 age of the U mineralizing events in the Guérande area (ca. 300 to 275 Ma) is comparable with

148 that in the Mortagne district, and with other U deposits from the EVB (Cathelineau et al. 1990;
149 Ballouard et al. 2017a). The Questembert leucogranite (Fig. 2) is not associated with U
150 mineralization but the petro-geochemical and geochronological study of Tartèse et al. (2013)
151 suggests that this intrusion liberated an important amount of uranium during a sub-solidus
152 alteration event at depth, by surface-derived oxidized fluids.

153 ***The Pontivy-Rostrenen magmatic complex.***

154 *General framework*

155 Gravimetric data reveals that the Pontivy-Rostrenen complex represents a continuous
156 intrusion with the main root (~6 km depth) localized to the north (Vigneresse and Brun 1983;
157 Vigneresse 1999). The southern part of the complex is composed almost exclusively of
158 peraluminous leucogranite, whereas peraluminous leucogranite and monzogranite outcrop to
159 the north with small stocks of mantle-derived metaluminous quartz monzodiorite (Fig. 3)
160 (Euzen 1993; Ballouard et al. 2017b). To the south, leucogranite intrudes Late-Proterozoic
161 (Brioverian) sedimentary rocks, whereas to the north leucogranit, monzogranite and quartz-
162 monzodiorite intrude Late-Proterozoic and Paleozoic (Ordovician to Lower Carboniferous)
163 sedimentary formations causing contact metamorphism (Fig. 3). Vigneresse (1999) estimated
164 that these intrusions were emplaced at a depth around 6 – 8 km. The shape of the Pontivy
165 leucogranite intrusion to the south marks the dextral shearing of the SASZ (Figs. 2 and 3) and,
166 in the southern edge, syn-cooling shearing is revealed by the development of C/S structures
167 (Gapais 1989) and mylonites in 100 m wide dextral shear zones, oriented N 100-110° (Jégouzo
168 1980). The oxygen isotope study carried out on mylonites from the Guilligomarch quarry (Fig.
169 3) in the southern edge of the complex showed that some of these rocks experienced
170 hydrothermal alteration by low $\delta^{18}O$ meteoric-derived fluids (Tartèse et al. 2012).

171 *Petrogeochemical characteristics*

The petro-geochemistry and geochronoly is summarized from Ballouard et al. (2017b). Leucogranite contains quartz-feldspar-muscovite with a variable amount of biotite that can be either absent or dominant over muscovite. Tourmaline is rarely observed. Common accessory minerals are zircon, apatite, monazite and Fe-Ti oxides. Uranium oxides were not observed in our samples. This absence is likely the consequence of the instability of this mineral during post-crystallization alteration and/or weathering, because uranium oxides were commonly observed in the drill cores from leucogranite associated with U deposits, such as Guérande (Oudou 1984) (Fig. 1), or in the northwestern part of theMassif Central (Friedrich et al. 1987). The leucogranite was divided into three main sub-facies (Fig. 3):

(1) The porphyritic leucogranite is characterized by the abundance of K-feldspar megacrysts and a higher amount of biotite over muscovite.

(2) The equigranular leucogranite represents the most common type of leucogranite in the complex, and is characterized by a low abundance (or the absence) of K-feldspar megacrysts. The proportion of biotite over muscovite is variable, biotite being even absent in some cases.

(3) The late equigranular leucogranite (Langonnet leucogranite) forms an elliptic stock which crosscuts the other facies. This leucogranite is rarely porphyritic and generally contains a low proportion of biotite.

In terms of alteration, chloritization of biotite is common and secondary muscovitization affects more particularly the muscovite > biotite equigranular facies. Several veins of pegmatite and aplite crosscut the leucogranite. Moreover, pegmatite stocksheider were described along the western edge of the late equigranular leucogranite and greisenization locally affects the most evolved parts of the equigranular and late equigranular leucogranites (Euzen 1993; Bos et al. 1997).

196 The monzogranite (Rostrenen granite) crops out in the northern part of the complex (Fig.
197 3). This facies contains a quartz-feldspar-biotite assemblage with a small amount of muscovite
198 and, locally, cordierite. The most common accessory minerals include zircon, monazite and Fe-
199 Ti oxides. Mafic enclaves with a composition similar to quartz-monzodiorite are commonly
200 observed in this facies (Euzen 1993). The quartz-monzodiorite facies mostly appears as small
201 stocks of a few km² in the eastern part of the monzogranitic intrusion (Fig. 3). This facies
202 generally contains quartz-feldspar-biotite-amphibole ± clinopyroxene as well as apatite,
203 titanite, zircon and Fe-Ti oxide as accessory minerals. Ocellar quartz is frequently observed in
204 this facies and interpreted as the result of a mixing with a felsic magma. Mingling features are
205 visible at the contact between the quartz-monzodiorite and the monzogranite.

206 U-Pb dating of magmatic zircon grains revealed that the three magmatic facies of the
207 complex were emplaced synchronously between 316.7 ± 2.5 Ma and 310.3 ± 4.7 Ma, whereas
208 the late equigranular leucogranite was emplaced later at 304.7 ± 2.7 Ma. The peraluminous
209 leucogranite (A/CNK > 1.1) has mostly sub-chondritic εNd(t) values (-4.79 to 2.08) and contain
210 numerous inherited zircon grains with Archean to Paleozoic ages. It formed by partial melting
211 of Neoproterozoic metasedimentary rocks and Paleozoic peraluminous orthogneisses. The
212 moderately peraluminous monzogranite (1.0 < A/CNK < 1.3) has a sub-chondritic εNd(t)
213 composition (-3.95 to -3.22), and contains magmatic zircon with sub-chondritic εHf(t) values
214 and scarce Paleozoic inherited zircon. It formed by partial melting of an orthogneiss with a
215 probable metaluminous composition. The metaluminous quartz monzodiorite (0.7 < A/CNK <
216 1.1) has sub-chondritic εNd(t) values (-3.19 to -2.17) and contains magmatic zircon grains with
217 sub- to slightly superchondritic εHf(t) values. It formed by partial melting of a metasomatized
218 lithospheric mantle.

219 The evolution from high (~70 wt.%) to very high (~75 wt.%) SiO_2 leucogranite is likely
220 explained by the fractional crystallization of a cumulate composed of Bt + Kfs + Pl as well as

accessory minerals such as Ap + Zrn + Mnz. The chemical evolution of monzogranite from high (~71 wt.%) to low (~65 wt.%) SiO_2 may reflect entrainment of peritectic minerals from the source (i.e. Cpx + Grt + Pl + Ilm) and/or a mixing with a mantle derived melt. The evolution of the quartz monzodiorite from ~ 54 wt.% to ~60 wt.% SiO_2 is likely the consequence of fractionation of a cumulate made of Pl + Bt + Cpx and mixing with a felsic magma with a probable monzogranitic composition.

U mineralization

Most of the U deposits in the Pontivy-Rostrenen complex (~2000 t of U extracted; IRSN 2004) are spatially associated with the equigranular leucogranite facies (Fig. 3). They are generally localized close to contact with the sedimentary country rock, or to micaschist enclaves (Marcoux 1982; Alabosi 1984; Cuney 2006). The most important U deposits occur as polyphase, commonly hematized, quartz veins mostly oriented N170° and interpreted as tension gashes accommodating dextral wrenching along the SASZ (Marcoux 1982; Alabosi 1984) such as the Bonote (~400 t U extracted) or the Kerlech-Lignol deposits (~1000 t U extracted; Fig. 3). A second type of U deposit, with a main orientation of N120-130°, occurs generally as brecciated quartz veins, such as in the Guern area where ~40 t U were extracted (e.g. Quistiave and Kerroch deposits), in relation with second order faults which also likely developed due to deformation along the SASZ (Marcoux 1982; Alabosi 1984). The third type corresponds to episyenite-hosted deposits such as in the Prat Mérrien and Poulprio area (~ 100 t U extracted; Fig. 3), where the mineralized bodies follow N130-160° oriented faults (Alabosi 1984). The episyenitization of leucogranite during hydrothermal alteration resulted in the dissolution of magmatic quartz, the destabilization of plagioclase, the development of secondary muscovite and the geodic crystallization of adularia, quartz, montmorillonite and carbonate, U being disseminated in clay or in major minerals (Alabosi 1984). A fourth type of deposits occurs as fracture fillings within Brioverian micaschist xenoliths (e.g., Kerségalec; Cuney 2006) (Fig. 3).

Analytical techniques

Whole-rock major and trace elements analyses

Three samples of episyenites collected by Alabosi (1984) in the Prat Mérrien and Poulprio quarries (Fig. 3) were crushed in the Géosciences Rennes Laboratory using agate mortars. Chemical analyses were performed by the Service d'Analyse des Roches et des Minéraux (SARM; CRPG-CNRS, Nancy, France) using an ICP-AES for major elements and an ICP-MS for trace elements following the techniques described in Carignan et al. (2001). The results of the whole-rock analyses are provided in Table 1.

Apatite chemistry and U-Pb dating

Apatite crystals from the different magmatic facies forming the complex as well as an episyenite sample were separated using classical magnetic and heavy liquid methods in the Géosciences Rennes Laboratory. Apatite grains were handpicked under a binocular microscope before being embedded in epoxy resin and polished. Apatite grains were imaged by cathodoluminesence (CL) using a Reliotron CL system in Géosciences Rennes (5 kV acceleration voltage and 600 µA beam current) and a Cambridge Image Technology (CITL) Mark 5 CL system at University of Mons, Belgium (15 kV acceleration voltage and 500 µA beam current). The CL system at UMons is also equipped with a CITL COS8200 fiber-based optical spectrometer with a 350-1100 nm spectral range and 4 nm resolution. Spectral calibration was performed with a standard Hg-Ar lamp. The spectra were not corrected for total system response. Backscattered electron (BSE) images and chemical maps were performed using the Cameca SX-100 electron probe micro analyze (EPMA) at IFREMER (Plouzané, France). Analyses were performed using a 15 keV accelerating voltage and a beam diameter of 15 µm. Beam currents of 10 nA and 20 nA were used for spot analyses and elemental mapping, respectively. Standards were: apatite (F Kα, TAP crystal, counting time of 30s; P Kα, LPET,

60s; Ca Kα, PET, 30s), albite (Si Kα, TAP, 30s; Na Kα, TAP, 30s), strontianite (Sr Lα, TAP, 30s), pyromorphyte (Cl Kα, LPET, 60s), Si-Al-Ca glass with 4w.% La (La Lα, LPET, 30s), barium sulfate (S Kα, PET, 30s), Si-Al-Ca glass with 4w.% Ce (Ce Lα, PET, 60s), andradite (Fe Kα, LLIF, 60s), rhodonite (Mn Kα, LLIF, 60s), gallium arsenide (As Lα, TAP, 60s).

U-Pb geochronology of apatite was conducted by in-situ laser ablation inductively coupled plasma mass spectrometry (LA-ICP-MS) at Géosciences Rennes using a ESI NWR193UC excimer laser coupled to a quadripole Agilent 7700x ICP-MS equipped with a dual pumping system to enhance sensitivity. The methodology used to perform the analyses can be found in Pochon et al. (2016) and in Electronic Material ESM1. Ages, calculated using the ISOPLOT software (Ludwig 2001), are provided with their 2σ uncertainties. All the isotopic ratios as well as the corresponding U and Pb contents in ppm are provided in ESM 2.

Uranium oxide U-Pb dating

Petrography and imaging of selected polished thin sections and mounts of uranium oxide samples were carried out at the GeoRessources Laboratory (Nancy, France) and the Centre de Recherches Pétrographiques et Géochimiques (CRPG, Nancy, France). U-Pb dating was carried out at the CRPG by secondary ion mass spectrometry (SIMS). The U oxide samples were first examined using reflected light microscopy. We then selected chemically homogeneous area with high radiogenic lead content suitable for SIMS analyses based on BSE images obtained using a JEOL J7600F, a HITACHI S-4800 (GeoRessources) or a JEOL 6510 (CRPG) scanning electron microscope and major element analyses obtained using a CAMECA SX100 EPMA (GeoRessources). U-Pb isotope analyses were performed using a CAMECA IMS 1270 SIMS. The complete methodology is described in ESM 3. Due to the common Pb-rich character of the U oxides ($50 < {}^{206}Pb/{}^{204}Pb < 11000$), a common lead correction based on the measured ^{204}Pb content and the Pb isotopic composition calculated using the model of Stacey and Kramers (1975) at the estimated age of the U oxide was applied to the analyses. All the isotopic ratios

295 are provided in ESM 4 and ages, calculated using the ISOPLOT software (Ludwig 2001), are
296 provided with their 2σ uncertainties.

297 # Results

298 ### *Uranium oxide petrography*

299 Uranium oxide U-Pb dating was performed on 6 mounts or thin sections belonging to the
300 AREVA collection from the Kerlech (Lignol), Rosglas and Quérrien (Kerjean) deposits as well
301 as three deposits in the region of Guern (Fig. 3: Quistiave, Kerroch and a sample referenced as
302 "undifferentiated-Guern" in the AREVA collection).

303 In the Guern region, the mineralization is described as brecciated quartz veins, following
304 N120 – 130° oriented faults, which mostly occur in tectonized contacts between the porphyritic
305 and equigranular leucogranites close to micashists enclaves and/or small stocks of quartz
306 monzodiorites (Marcoux 1982; Cuney 2006) (Fig. 3). The Quistiave deposit consists of two
307 veins orientated WNW-ESE and dipping SW, occurring about 80 m apart. The veins are more
308 or less parallel to alternating bands of a porphyritic biotite-rich – muscovite granite and an
309 equigranular muscovite-rich and biotite-poor leucogranite, and minor pegmatite veins. The
310 uranium mineralization occurs as discontinuous lenses along these structures and has been
311 mined to a depth of 95 m. The wall zone of the vein is made by a ~1 cm thick quartz comb
312 where U oxide nodules (up to 50 cm in diameter) have grown. The center part was, then, filled
313 by brecciated quartz, chalcopyrite, galena, sphalerite, marcasite, covellite and bismuthinite
314 (Cuney 2006). The analyzed sample corresponds to a nodule of pseudo-spherulitic to spherulitic
315 U oxide (Ur1) brecciated by microfractures mainly filled with quartz, chalcopyrite, galena,
316 sphalerite and a product of alteration of Ur1 (Alt Ur1; Fig. 4a). In the sample from the Kerroch
317 deposit, the mineralization occurs as clusters of millimeter sized spherulitic U oxides
318 disseminated in a leucogranitic granitic country rock and crosscut by ~10 µm wide veins filled

with quartz and sulfides (Fig. 4b). In the last sample from the Guern region (undifferentiated-Guern, Fig. 4c), 0.05 to 2 mm wide veins filled by quartz and spherulitic to pseudo-spherulitic U oxide crosscut the leucogranitic country rock.

In the Kerlech (Lignol) deposit, 50 cm to 1 m wide mineralized quartz veins oriented N-S to N°170 crosscut the equigranular leucogranite from the contact with the sedimentary rocks (Marcoux 1982; Cuney 2006) (Fig. 3). Vein filling began with a quartz comb followed by fine grained quartz bearing U oxide and chalcopyrite. The last infilling event is represented by barren quartz (Cuney 2006). In the studied sample, a centimeter large cluster of U oxide spherules (Ur1) up to 500 µm in length occurs in fine grained (< 1 mm) quartz together with Fe oxides. The first generation of spherulitic U oxide (Ur1) is brecciated by a second generation of U oxide (Ur2) accompanied by quartz, galena and locally bismuthinite (Fig. 4d).

Rosglas and Quérrien (Kerjean) are both classified as episyenite type deposits and are found in the equigranular leucogranite facies (Fig. 3). At Rosglas the episyenite forms a nearly cylindric subvertical column at the intersection of two faults. In the Rosglas sample, the mineralization occurs as millimeter large clusters of U oxide spherules, with a diameter of 10 to 100 µm, disseminated in episyenitized leucogranitic country rocks (Fig.4e). In the Quérrien (Kerjean) sample, the mineralization occurs as brecciated millimeter-wide pseudo-spherulitic U oxides veinlets or clusters disseminated in episyenitized leucogranitic country rocks. In the BSE images, U oxides, crosscut by numerous millimeter-wide fractures, are characterized by the presence of light grey zones interpreted as unaltered (Ur1) and dark grey zones interpreted as altered U oxide (Alt Ur 1; Fig. 4f).

Uranium oxide U-Pb dating

Chemically homogeneous areas that had undergone little or no post-crystallization alteration were selected for U-Pb SIMS dating (Fig. 4). Yet, most analyses plot in a discordant

position in the Wetherill concordia diagram (Wc) (Fig. 5), suggesting radiogenic Pb losses which could be the result of hydrothermal alteration (Fig. 4).

For the Quistiave (Guern) deposit (Fig. 5a), the 8 analyses plot in a discordant position in the Wc diagram and define a poorly constrained upper intercept of 290 ± 69 Ma (MSWD = 4.1) and a lower intercept of 7 ± 130 Ma. If the discordia is anchored at 0 Ma, assuming a recent Pb loss, an upper intercept of 286 ± 10 Ma (MSWD = 3.5) is obtained. For the Kerroch (Guern) deposit (Fig. 5b), the 30 analyses are discordant to concordant and display an important scattering in the Wc diagram. A poorly constrained upper intercept of 307 ± 86 Ma (MSWD = 1.3) and a lower intercept of 89 ± 66 Ma are obtained. For the last sample from the Guern region deposits (Guern – undifferentiated; Fig. 5c), the 15 discordant analyses, affected by Pb loss, define a relatively well-constrained upper intercept of 268 ± 8 Ma (MSWD = 1.2) and a lower intercept of -15 ± 24 Ma in the Wc diagram. Assuming a recent Pb loss, an upper intercept of 273 ± 3 Ma (MSWD = 1.2) can be calculated. For the Kerlech (Lignol) deposit (Fig. 5d), the 13 analyses plot in a discordant position and display an important scattering in the Wc diagram. The data define a poorly constrained upper intercept of 258 ± 89 Ma (MSWD = 1.3) and a lower intercept of -18 ± 210 Ma. If the discordia is anchored at 0 Ma in the Wc diagram, an upper intercept of 267 ± 11 Ma (MSWD = 1.2) is obtained. Regarding the sample from the Rosglas deposit (Fig. 5e), the 12 discordant analyses, affected by Pb loss, define a relatively well-defined upper intercept of 303 ± 32 Ma (MSWD = 0.5) and a lower intercept of 33 ± 130 Ma. A comparable upper intercept of 296 ± 4 Ma (MSWD = 0.5) is obtained by anchoring the discordia at 0 Ma. Finally, for the Quérrien (Kerjean) deposit, the 14 analyses plot in concordant to discordant positions in the Wc diagram reflecting variable degree of Pb loss (Fig. 5f). The data define a well-constrained upper intercept of 219 ± 5 Ma (MSWD = 0.9) with a lower intercept of -8 ± 69 Ma. By anchoring the discordia at 0 Ma, an identical upper intercept of 219 ± 5 Ma (MSWD = 0.8) is obtained.

368 ***Whole-rock geochemistry and U-Th distribution***

369 Some major element compositions of whole-rock samples from the Pontivy-Rostrenen
370 complex are reported in the Q-P diagram (Fig 6a). Leucogranite, monzogranite and quartz
371 monzodiorite plot mostly in the field defined for granite-adamellite, ademellite and quartz
372 monzodiorite, respectively, whereas the episyenite sample from the Prat Mérrien deposit plots
373 in the granite field and the two episyenite samples from the Poulprio deposit plot out of the field
374 defined for magmatic rocks. The episyenites, which result from leucogranite metasomatism
375 (Alabosi 1984), display evidence of an important dequartzification combined with potassic
376 alteration for Poulprio and a slight dequartzification for Prat Mérrien (Fig. 6a). Loss on ignition
377 (LOI) between ~4 and 8 wt.% in the episyenite samples reflects the presence of carbonates and
378 clay minerals (montmorillonite; Alabosi 1984), whereas LOI are below 2 wt.% for the unaltered
379 leucogranite. The episyenite sample from Part Mérrien is also enriched in P_2O_5 (1.19 wt.%;
380 Table 1) compared to other episyenites (P_2O_5 < 0.7 wt.%; Table 1) and unaltered leucogranite
381 samples (P_2O_5 < 0.5 wt.%; Ballouard et al. 2017b). Moreover, all episyenite samples display
382 higher As content relative to leucogranite with values from 20 to 95 ppm (Table 1) in
383 episyenites whereas the As content in leucogranite is generally below 11 ppm (Ballouard et al.
384 2017b).

385 In the Th vs. U diagram (Fig. 6b), monzogranite and quartz monzodiorite samples are
386 characterized by high Th/U values mostly above 3, low U contents from ~3 to 9 ppm and a
387 poorly-defined correlation between Th and U. In contrast, the Th/U ratios and U contents are
388 highly variable in the leucogranite and range from ~0.1 to 5 and ~3 to 27 ppm, respectively.
389 Among leucogranite, the lowest Th/U ratios (< 1) and highest U contents (> 15 ppm) are
390 displayed by the equigranular leucogranite and the late equigranular leucogranite whereas Th/U
391 ratios above 1 and U contents below or equal to 15 ppm are found in the porphyritic
392 leucogranite. U correlates negatively with Th for the late equigranular leucogranite samples

393 whereas no clear correlation appears for the porphyritic and equigranular leucogranite. In the
394 episyenite, the Th/U ratios range from 0.9 to 0.01 with a U content from 17 to 48 ppm for
395 Poulprio and of 113 ppm for Prat Mérrien. The Prat Mérrien episyenite is characterized by an
396 extremely low Th content of 0.6 ppm.

397 ***Apatite petro-geochemistry***

398 Apatite is a common accessory mineral in all the magmatic rocks from the Pontivy-
399 Rostrenen complex. In this study, chemical analyses (Table 2) were performed on separated
400 apatite grains from one porphyritic leucogranite (PONT-1: 13 grains), two equigranular
401 leucogranites (PONT-10: 13 grains, PONT-26: 14 grains), the late equigranular leucogranite
402 (PONT-20: 13 grains), one episyenite (MS-81-66-PM: 10 grains), one monzogranite (PONT-
403 22: 20 grains) and two quartz-monzodiorites (PONT-7:14 grains, PONT-23: 15 grains). In all
404 these samples, the F content in the apatite crystals is always above 0.75 apfu indicating that
405 they are fluoroapatite (Table 2).

406 In all leucogranite and episyenite samples, apatite grains appear as squat prisms up to 500
407 µm in length. In leucogranite, the crystals display generally yellow-green colors in
408 cathodoluminescence (CL) with irregular patchy zoning (Fig. 7a) not visible in the BSE images.
409 In these CL images, the dark yellow-green color characteristic of the grain cores generally
410 evolves toward light yellow-green or even locally blue colors for the rims. CL emission spectra
411 reveal mainly Mn^{2+} and minor REE^{3+} activated luminescence in both yellow-green zones (Fig.
412 8a). The change from dark yellow-green to light yellow-green color is associated with a
413 decrease in the Fe and Mn contents in the chemical maps (Fig. 7a) and in the Mn vs. Fe diagram
414 (Fig. 9), suggesting that the decrease of the CL intensity is due to quenching of Mn-activated
415 CL by Fe or self-quenching effect by Mn (Kempe and Götze 2002). In samples PONT-10 and
416 26, the cores are characterized by Mn and Fe contents from 0.04 to 0.17 and 0.02 to 0.07 apfu,
417 respectively, whereas in the rims, the Mn and Fe contents range from < 0.01 to 0.11 and < 0.01

418 to 0.06 apfu, respectively (Fig. 9). In the episyenite samples, apatite crystals commonly display
419 irregular zoning with yellow-green, blue, blue-grey or red-pink colors in CL images (Fig 7b).
420 Blue-grey CL zones are commonly observed as overgrowth or as patches and veins in yellow-
421 green and blue zones whereas red-pink zones are observed as late overgrowth for the other
422 zones (Fig. 7b). CL spectra reveal mainly Mn^{2+} with minor Eu^{2+} and REE^{3+} activated
423 luminescence in yellow-green zones whereas the CL activation by both Eu^{2+} and REE^{3+}
424 increases in the other zones (Fig. 8b). As seen on the spectra, the differences in CL color in
425 these apatite grains result from subtle changes in the emission caused by three main activators:
426 Eu^{2+} (blue), Mn^{2+} (yellow-green) and Sm^{3+} (red). Interestingly, the CL spectra in blue, blue-
427 grey and red-pink zones commonly show activation by Eu^{3+} (Fig. 8b). Crystals or zones with a
428 yellow-green color in the CL images are generally characterized by elevated Mn and Fe
429 contents from 0.08 to 0.12 and 0.03 to 0.04 apfu, respectively, whereas blue (and blue-grey)
430 CL zones display Fe and Mn contents < 0.01 apfu (Fig. 9). In contrast, the REE content as
431 indicated by La and Ce concentration does not significantly change (Table 2), suggesting that
432 the increased REE activation in blue and blue-grey CL zones relative to yellow-green CL zones
433 is not due to an increase in REE concentration but rather to a decrease in Mn^{2+}. Zones with a
434 red-pink color in CL images are brighter in the BSE images (Fig. 8b) and are characterized by
435 Fe and Mn below detection limit, an elevated average As content of 0.28 apfu (commonly <
436 0.01 apfu in other grains) and an elevated average OH content of 0.21 apfu (generally around
437 0.1 in other crystals; Table 2). There is a perfect match between dark red CL and As-rich bands
438 (Fig. 7b). Incorporation of As in apatite structure likely explains the decrease of CL intensity
439 since As has been reported as a CL inhibitor (Perseil et al. 2000; Kempe and Götze 2002). The
440 combined increase in both As and OH contents marks the evolution toward the johnbaumite
441 end-member [$Ca_5(AsO_4)_3(OH)$].

In the monzogranite sample, apatite appears as squat or elongated prisms up to 500 µm in length homogeneous in BSE images and displaying a generally homogeneous yellow-green CL color (Fig. 7c). CL spectra reveal a major Mn^{2+} with a moderate REE^{3+} activated luminescence (Fig. 8c). Rarely, apatite grains display a zonation on Si chemical map with a slight decrease of the Si contents from core (~0.02 apfu) to rim (< 0.01 apfu) (Fig. 7c). The Mn (0.02 – 0.03 apfu) and Fe (0.01 – 0.03 apfu) contents are generally lower than those found in the apatite grains from the leucogranite (Fig. 9). Regarding the quartz monzodiorite samples, apatite crystals appear as squat or elongated prisms up to 200 µm in length. These apatite crystals appear as homogeneous in BSE images and display a predominant purple CL color with purple-green rims (Fig. 7d). CL emission spectra reveal a major REE^{3+} and Eu^{2+} with minor Mn^{2+} activated luminescence. Here again, slight changes in spectra have an impact on the resulting CL color, with the more greenish CL being induced by a decrease in Sm^{3+} (red) relative to Dy^{3+} (green) Accordingly, EPMA analyses show a slight decrease of the LREE content ([La + Ce] ~0.01 apfu to below detection limits) from core to rim and these crystals are characterized by low Fe and Mn contents below 0.01 apfu (Fig. 9). Note that here the emission peak at 415 nm (Fig. 8d) could be related to structural defects associated with REE substituting for Ca^{2+} (Marshall 1980) as Eu^{2+} emission occurs at about 450 nm (e.g. Blanc et al. 2000) as it is the case in episyenite apatite (Fig. 8b).

Apatite U-Pb dating

Apatite U-Pb analyses were performed for all the samples presented in the last section with the exception of the quartz monzodiorite PONT-23. The results are reported in Tera-Wasserburg diagrams (Fig. 10).

In leucogranite, the analyses are discordant with $^{207}Pb/^{206}Pb$ ratios ranging from 0.148 to 0.537. Due to the small size of the rims observed in the CL images, analyses were almost exclusively performed on grains cores. For the porphyritic leucogranite sample PONT-1 (Fig.

10a), 23 analyses on 19 different grains define a poorly defined lower intercept of 285.4 ± 8.5 Ma (MSWD = 6.8). Using the common Pb composition calculated at 285 Ma (Stacey and Kramers 1975), the analyses yield two populations for the ^{207}Pb corrected ages; 307.2 ± 7.1 Ma (MSWD = 2.2, n = 9) and 286.2 ± 3.8 Ma (MSWD = 1.6, n = 14), respectively. For the equigranular leucogranite sample PONT-10 (18 analyses from 16 grains; Fig. 10b), the unforced discordia yields a lower intercept of 270.4 ± 6.7 Ma (MSWD =2.5). Once again, two populations are obtained for the corrected ^{207}Pb ages, calculated using the common Pb composition at 270 Ma, and yield mean values of 294.9 ± 7.4 Ma (MSWD = 0.12) and 279.9 ± 2.9 Ma (MSWD = 0.42), respectively. For the equigranular leucogranite PONT-26 (21 analyses from 15 grains; Fig. 10c), we obtain a lower intercept of 272.8 ± 2.9 Ma (MSWD = 1.2). Two populations of ^{207}Pb corrected ages are obtained and yield mean values of 299.9 ± 4.3 Ma (MSWD = 0.26) and 279.6 ± 2.1 Ma (MSWD = 0.59), respectively. Then, for the late equigranular leucogranite sample (PONT-20; 24 analyses from 18 grains; Fig. 10d), a poorly constrained lower intercept at 278.0 ± 11.0 Ma (MSWD = 8.7) is obtained and analyses yield two populations of ^{207}Pb corrected ages with a mean value of 297.1 ± 3.0 Ma (MSWD = 1.6) and 280.9 ± 2.1 Ma (MSWD = 0.63), respectively. There is no clear correlation between the apparent ^{207}Pb corrected ages obtained for the apatite grains from leucogranite and their relative Mg and/or Fe contents.

For the episyenite sample (MS-81-66-PM; Fig. 10e), the discordant analyses display highly variable common Pb contents with ^{207}Pb/^{206}Pb values ranging from 0.122 to 0.861. No analyses were performed on the blue-grey or pink-red CL zones because of their small sizes. In this sample, 9 analyses out of 6 grains presenting yellow-green or blue colors and characterized by ^{207}Pb/^{206}Pb values below 0.300, display a well-defined discordia and yield a lower intercept age of 289.0 ± 10.0 Ma (MSWD =0.54). This age is identical within error to the mean ^{207}Pb

corrected age of 286.5 ± 3.8 Ma (MSWD = 0.31). The other data characterized by a higher common Pb content are more scattered and were therefore not used.

Regarding the monzogranite sample (PONT-22; Fig. 10f), the 23 analyses from 22 grains are discordant with $^{207}Pb/^{206}Pb$ values ranging from 0.268 to 0.729. The analyses yield a well-defined lower intercept of 317.8 ± 4.9 Ma (MSWD = 1.2) identical within error to a mean ^{207}Pb corrected age of 320.6 ± 3.1 Ma (MSWD = 0.76).

Finally, for the quartz-monzodiorite sample (PONT-7; Fig. 10g), the 17 analyses from 13 grains are discordant with $^{207}Pb/^{206}Pb$ values from 0.316 to 0.628. The data align on a discordia which yields a well-defined lower intercept of 298 ± 13 Ma (MSWD = 1.17) identical within error to a mean ^{207}Pb corrected age of 310.4 ± 7.5 Ma (MSWD = 0.31).

Discussion

U behavior in the Pontivy-Rostrenen complex

In contrast to the quartz monzodiorite and monzogranite samples, characterized by low U contents (< 9 ppm) and elevated Th/U values mostly above 3, the leucogranite is characterized by both highly variable U contents (~3 to 27 ppm) and Th/U ratios (~0.1 to 5) (Fig. 6b). The Th/U is an indicator of the nature of the U bearing minerals in granitoids and the high Th/U ratios (> 2) measured in some samples suggest that most of their U is hosted in refractory mineral phases such as zircon, titanite or allanite for quartz monzodiorites and zircon or monazite for leucogranite and monzogranite (Cuney 2014). On the other hand, low Th/U values (< 1) and U contents of tens of ppm in peraluminous leucogranitic melts favor the crystallization of magmatic uranium oxides at the expense of monazite and up to 80-90 % of the available U can be hosted in U oxide (Friedrich et al. 1987; Peiffert et al. 1994, 1996; Förtser 1999; Förster et al. 2008; Cuney 2014). In leucogranitic magmas, extraction of accessory minerals incorporating limited amounts of U, such as monazite and zircon, during fractional

515 crystallization (Ballouard et al. 2017b) likely induced an increase of the U contents in the melt
516 and a decrease of the Th/U values. Such behavior, well-illustrated by the negative correlation
517 between Th and U in the late equigranular leucogranite (Fig. 6b), probably triggered the
518 crystallization of uranium oxides in the most evolved leucogranitic melts. In contrast, there is
519 no correlation between Th and U for the porphyritic and equigranular leucogranites (Fig. 6b).
520 We propose that the very variable Th/U values displayed by these facies can be attributed to a
521 combination between magmatic evolution (uranium oxides crystallization), hydrothermal
522 alteration and/or surface weathering (uranium oxides leaching), low Th uranium oxides being
523 particularly prone to dissolution by infiltrating oxidized fluids (Förster 1999, Förster et al.
524 2008). In the episyenite sample, the high U contents suggest hydrothermal U enrichment while
525 the extremely low Th content of the Prat Mérrien sample suggest either high degree of magmatic
526 fractionation or monazite leaching, the latter being documented in some episyenites (López-
527 Moro et al. 2013).

528 ***Age of the uranium mineralization***

529 U-Pb analyses of uranium oxides provide evidence for a complex behavior of the U-Pb
530 system depending on the samples. A first group composed of the Guern-undifferentiated,
531 Rosglas and Quérrien (Kerjean) samples yield relatively well-constrained, unforced upper
532 intercepts of 268 ± 8 Ma, 303 ± 32 Ma and 219 ± 5 Ma, respectively whereas the Quistiave
533 (Guern), Kerroch (Guern) and Kerlech (Lignol) samples, belonging to the second group, yield
534 poorly constrained unforced upper intercepts of 290 ± 69 Ma, 307 ± 86 Ma and 258 ± 89 Ma
535 respectively (Fig. 5). In Figure 11, the analyses from the two groups are reported in a $^{206}Pb/^{207}Pb$
536 versus $^{235}U/^{207}Pb$ concordia diagram that is useful to discriminate between Pb loss and Rn
537 leakage processes in uranium oxides (Ludwig and Simmons 1992). In this diagram, samples
538 from the first group only display evidence of Pb loss whereas samples from the second group
539 display evidence for both Pb loss and Rn leakage. It is not possible to constrain precisely the

timing of the Rn leakage in these samples but this process seems to have occurred during the Mesozoic (Fig. 11b). In contrast, unforced lower intercept ages close to 0 suggest recent Pb loss for all samples excepted Kerroch (Guern: Fig. 5). Therefore, we suggest that the poorly constrained upper intercept U-Pb ages obtained for samples from the second group are the result of a complex combination of Pb loss and Rn leakage. Despite that the Wc diagrams suggest an Upper Carboniferous to Lower Permian age for the crystallization of these samples (Fig. 5), we argue in the followings that only the samples from the first group (Fig. 11a) can be used to constrain precisely the timing of the U mineralizing events in the Pontivy-Rostrenen district.

In the Guern region, the Guern-undifferentiated sample yields an unforced upper intercept age of 268 ± 8 Ma which is identical within error to the upper intercept of 273 ± 3 Ma obtained if the discordia is anchored at 0 Ma (Fig. 5c). Therefore, we suggest that this deposit formed 273 ± 3 Ma ago. Analyses on uranium oxides from the Rosglas deposit yield an unforced intercept of 303 ± 32 Ma identical within error to the forced upper intercept age of 296 ± 4 Ma that we interpret as the age of formation (Fig. 5e). Then, the U oxides from the Quérrien (Kerjean) deposit yield two identical well-constrained upper intercepts of 219 ± 5 Ma (Fig. 5f), interpreted as the age of their crystallization. To sum up, the hydrothermal U deposits from the Pontivy-Rostrenen complex mostly formed during the Lower Permian, from ca. 300 to 270 Ma, but some U deposits formation or U remobilization also occurred during the Triassic around 220 Ma as illustrated in the Quérrien (Kerjean) deposit.

Apatite as a proxy to date emplacement and/or alteration ages?

Apatite dating in rocks unaffected by fluids

In the quartz monzodiorite and the monzogranite, apatite grains are unzoned or display discrete regular zonation on CL images (Fig. 7c and d), which suggest that these crystals have kept their magmatic signature and were not affected by significant hydrothermal processes. U-

564 Pb dating of apatite grains from the quartz monzodiorite yield a lower intercept of 298.0 ± 13.0
565 Ma identical within error to a mean ^{207}Pb corrected age of 310.4 ± 7.5 Ma (Fig. 10g). The mean
566 ^{207}Pb corrected age is identical within error to the zircon U-Pb age of 315.2 ± 2.9 Ma obtained
567 for this facies (Ballouard et al. 2017b) (Table 3), and can be interpreted as reflecting the
568 emplacement for this quartz-monzodiorite intrusion. In the monzogranite, apatite grains provide
569 comparable intercept and mean ^{207}Pb corrected ages of 317.8 ± 4.9 Ma and 320.6 ± 3.1 Ma (Fig.
570 10f), respectively. Both ages are identical within error to the zircon U-Pb age of 315.5 ± 2.0
571 obtained on this sample (Ballouard et al. 2017b) (Table 3) and can be interpreted as reflecting
572 the emplacement age of the intrusion.

573 *Apatite dating in rocks affected by fluids*

574 In contrast to the monzogranite and quartz monzodiorite apatite crystals, the apatite grains
575 from leucogranite and episyenite display petro-geochemical evidence for pervasive
576 hydrothermal alteration. Indeed, these apatite grains show patchy irregular zoning in the CL
577 images and in the Fe and Mn chemical maps, likely reflecting fluid interactions processes
578 (Fig.7a). The decrease in the Mn and Fe contents, generally observed from the core to the rims
579 (Fig. 7a and 9) likely reflects the transition toward a more oxidized environment during
580 hydrothermal events. Indeed, Mn and Fe are more compatible in apatite in reduced conditions
581 as Mn^{2+} and Fe^{2+} substitute easily to Ca^{2+} (Miles et al. 2014). In addition to the irregular patchy
582 zoning reflecting Fe and Mn mobility, apatite grains from the episyenite also display features
583 likely hydrothermal in origin. The formation of new apatite is in agreement with the elevated
584 whole-rock P content (1.2 wt.%) measured for this sample (MS-81-66; Table 1). Late apatite
585 overgrowths, having a red-pink color in CL images, show enrichment in As and OH
586 characteristic of a substitution toward the johnbaumite end-member (Fig. 7b). The observed
587 OH enrichment suggests that these zones crystallized in a H_2O-rich environment whereas the
588 increase of the As content reflects the high oxygen fugacity of the hydrothermal fluids as As^{5+}

589 will substitute more easily for P^{5+} than As^{3+}. Moreover, apatite zones interpreted as
590 hydrothermal in origin (blue, blue-grey or red-pink CL zones in episyenite sample MS-81-66;
591 Fig 7b) show a slight but significant Eu^{3+} activation (Fig. 8b) that could also be interpreted as
592 related to the oxidized character of the mineralizing fluid (Roeder et al. 1987; Mitchell et al.
593 1997). Roder et al. (1987) argued that no conclusive interpretation regarding the redox state of
594 the fluids can be drawn from the observation of Eu^{3+} activation in the CL of apatite because
595 apatite is expected to concentrate preferentially Eu^{3+} over Eu^{2+}. However, in our episyenite
596 apatite, the involvement of oxidized fluids is supported by the occurrence of As^{5+} and the
597 observed Eu^{3+} activation could be regarded as an additional evidence.

598 In the episyenite sample MS-81-66 (Fig. 10e), apatite grains yield a lower intercept of 289.0
599 ± 10 Ma and a mean ^{207}Pb corrected of 286.5 ± 3.8 Ma identical within error. Considering the
600 alteration evidence depicted above, we thus argue that dating of these apatite grains provides
601 the age of the episyenitization (i.e. the metasomatism of the leucogranite) at 286.5 ± 3.8 Ma.

602 In each of the leucogranite samples, the data obtained by apatite U-Pb dating reveal a
603 complex behavior with regard to their U-Pb system. First of all, the lower intercept obtained
604 for leucogranite are characterized by rather high MSWD values (between 2.5 and 8.7) with the
605 exception of equigranular leucogranite PONT-26 (MSWD=1.2). This probably means that the
606 scattering of the data can be attributed to geological event(s) rather than to an analytical
607 problem. This is further amplified by the fact that lower intercept and ^{207}Pb corrected ages are
608 systematically different and, when available, are always younger than the emplacement ages
609 (Ballouard et al. 2017b; see Table 3). As outlined earlier, all the apatite grains from leucogranite
610 show evidence for some interaction with fluids. At a first order, this means that the U-Pb system
611 in these grains has been affected by late fluid circulations. In all cases, the mean ^{207}Pb corrected
612 ages define two different populations for each sample: a first one returning ages in the range
613 294.9 ± 7.4 Ma to 307.2 ± 7.1 Ma, and a second one with ages ranging from 279.6 ± 2.1 Ma to

614 286.2 ± 3.8 Ma (Fig. 10a-d). In Figure 12, the calculated U contents in the apatite grains are
615 reported as a function of the corresponding ^{207}Pb corrected ages. Regarding the apatite grains
616 from the monzogranite ([U] ~7 – 90 ppm), quartz-monzodiorite ([U] ~12 – 56 ppm), late
617 equigranular leucogranite ([U] ~48 – 184 ppm) and episyenite ([U] ~95 – 263 ppm) samples,
618 the U content is relatively constant and there is no correlation with the ^{207}Pb corrected ages. In
619 contrast, the U contents in the apatite from the equigranular (and the porphyritic leucogranite)
620 increase as the ^{207}Pb corrected ages get younger. This inverse correlation between the apatite
621 grain apparent ages and their U contents likely shows that the fluids which interacted with these
622 apatite grains were U-rich.

623 In order to determine if we can extract meaningful ages from this dataset, we decided, for
624 each sample, to keep only the population returning the youngest ^{207}Pb-corrected ages (Fig. 13).
625 The resulting unforced lower intercept ages are 285.9 ± 7.4 Ma (MSWD=2.1; PONT-1:
626 porphyritic leucogranite), 266 ± 11 Ma (MSWD=2.7; PONT-10: equigranular leucogranite),
627 272.8 ± 6.4 Ma (MSWD=0.39; PONT-26: equigranular leucogranite) and 278 ± 15
628 (MSWD=0.84; PONT-20: late equigranular leucogranite). Individually, all these ages are
629 comparable with their respective ^{207}Pb-corrected ages. We therefore conclude that the youngest
630 mean ^{207}Pb-corrected ages represent, for each sample, the best estimate of the time when the
631 fluids interacted with the rocks. The other, older, ages probably represent partially reset apatite
632 grains and are therefore meaningless.

633 As a conclusion, apatite U-Pb dating of episyenite and leucogranite provide evidence for
634 fluid infiltration from ca. 290 Ma (episyenitization) to 275 Ma (late alteration of leucogranite).
635 This period is contemporaneous with the Lower Permian ages obtained on most of the uranium
636 deposits in the Pontivy-Rostrenen district (Fig. 5). This, together with the fact that the apatite
637 grains affected by the fluids are richer in uranium than those that have been partly affected, or

not-affected, suggest that these hydrothermal fluids were the same than those at the origin of the formation of U deposits (Fig. 12).

Metallogenic model and regional implication

In the Pontivy-Rostrenen complex, the main U mineralization is hosted in N170° oriented quartz veins (Kerlech – Lignol, Bonote) or as brecciated quartz veins (Guern region) and episyenite bodies (Prat Mérrien, Poulprio) where the mineralized zone follows N120-130° and N130-160° oriented brittle lineaments, respectively. As illustrated in Figure 14 and proposed by Marcoux (1982), the N170° oriented mineralized quartz veins can be interpreted as tension gashes accommodating late dextral movement along the SASZ, whereas the formation of other deposits could be related to second order faulting also associated with deformation along the SASZ. Muscovite Ar-Ar and zircon or monazite U-Th-Pb dating on syntectonic leucogranite and mylonites from the SASZ (Tartèse et al. 2011b; 2012; Gapais et al. 2015) bracketed the ductile deformation along the SASZ between ca. 315 and 300 Ma. According to uranium oxide and apatite U-Pb dating on U deposits and leucogranite from the Pontivy-Rostrenen complex, respectively, brittle deformation which allowed the mineralizing fluids to circulate was active from ca. 300 to 270 Ma.

On a regional scale, U deposition in the Pontivy-Rostrenen complex was contemporaneous with U mineralizing events in the Mortagne (from ca. 290 to 260 Ma; Cathelineau et al. 1990) (Fig 2) and Guérande (from ca. 300 to 275 Ma; Ballouard et al. 2017a; Figs. 2 and 14) districts. In the Guérande district, the main perigranitic vein mineralization (Pen Ar Ran) occurs in a graben structure localized above the apical zone of the Guérande leucogranite. The formation of the graben and U mineralization relates to a brittle-ductile deformation which followed the emplacement of the Guérande intrusion in an extensional setting at ca. 310 Ma (Ballouard et al. 2015, 2017a) (Fig. 14). From 310 to 300 Ma, the SASZ acted as a transfer zone between the South Armorican Massif, a thickened domain in extension, and the Central Armorican Massif,

663 a thin domain under pervasive dextral wrenching (Gumiaux et al. 2004a; Gapais et al. 2015).
664 According to uranium oxide U-Pb dating, this tectonic configuration was likely active until the
665 middle Permian under mostly brittle conditions. U deposition in the Armorican Massif is
666 contemporaneous with the main U mineralizing phase in the whole EVB (300 – 260 Ma;
667 Cathelineau et al. 1990; Tischendorf and Förster 1994; Romer et al. 2010; Ballouard et al.
668 2017a) and follow the main period of formation of W ± Sn granite-related deposits in the Massif
669 Central (Fig. 1) that mostly occurred from ca. 335 to 300 Ma (Harlaux et al. 2017).

670 As outlined earlier, the apatite grains from leucogranite of the Pontivy-Rostrenen complex
671 and their episyenites show evidence for an interaction with oxidized hydrothermal fluids from
672 ca. 290 to 275 Ma, contemporaneous with the formation of the U deposits. A surface-derived
673 origin is favored as numerous indications for the infiltration of meteoric-derived fluids at depth,
674 from oxygen isotopes and fluid inclusions studies, exist in rocks associated with the SASZ:
675 quartz veins (Lemarchand et al. 2012), leucogranite (Tartèse and Boulvais 2010) and mylonite
676 (Tartèse et al. 2012). For example, a mylonite from the Guillomarch quarry on the southern-
677 edge of the Pontivy-Rostrenen complex (Fig. 3) displays whole-rock $\delta^{18}O$ values as low as 1.7
678 ‰, which indicates interaction with a low-$\delta^{18}O$ fluid derived from the surface (Tartèse et al.
679 2012). Surface-derived fluids, likely oxidized, are thus able to transport an important quantity
680 of U in solution (Dubessy et al. 1987). During the late Carboniferous and Early Permian, the
681 SASZ and the detachments likely acted as major channels for surface-derived oxidized fluids
682 which have the capacity to dissolve magmatic uranium oxides in fertile intrusions such as the
683 Guérande (Ballouard et al. 2017a), Questembert (Tartèse et al. 2013) and the Pontivy-Rostrenen
684 leucogranites (Fig. 14).

685 In the Guérande district (Figs. 2 and 14), fluid inclusion analyses of a quartz from a quartz-
686 uranium oxide vein of the Pen Ar Ran deposit, indicate a low salinity mineralizing fluid (1-6
687 wt.% eq. NaCl) with trapping temperatures in the range 250 – 350 °C (Ballouard et al. 2017a).

688 The trapping temperatures and the salinities of fluid inclusions in the Guérande district are
689 overall comparable with those obtained in U deposits from the Mortagne district (Fig. 2) and
690 the northwestern part of the Massif Central (Fig. 1), with salinity and temperature generally in
691 the range 0 – 7 wt.% eq. NaCl and 150-250 °C, respectively (Cathelineau 1982; Cathelineau et
692 al. 1990; Lespinasse and Cathelineau 1990; Cuney and Kyser 2008). The low salinity measured
693 in the fluid inclusions from these deposits are in agreement with the contribution of meteoric-
694 derived fluids although the elevated trapping temperatures and the variation of salinity values
695 suggest mixing processes with metamorphic- or basin-derived fluids, as it was already proposed
696 for the FMC (Turpin et al. 1990) and the Bohemian Massif (Kříbek et al. 2008; Dolníček et al.
697 2013).

698 In the Guérande district, the uranium precipitated at the contact with reducing lithologies,
699 such as black shales (Cathelineau et al. 1981; Ballouard et al. 2017a). In the Pontivy-Rostrenen
700 district, most deposits occurred to the north of the Pontivy intrusion close to the contact with
701 sedimentary country rocks or micaschists enclaves, which likely played a role in the U
702 precipitation processes. In parallel, regional-scale strike slip faults can act as channels for lower
703 crustal reduced metamorphic fluids, in addition to surface derived fluids, such as those
704 documented in regional quartz veins along the SASZ (Lemarchand et al. 2012). These fluids
705 can in turn be involved in U precipitation (Fig. 14). Permian basins are not preserved in the
706 Armorican Massif, with the exception of its northeastern part where shales and red sandstones
707 were deposited in fluvial or lacustrine environments (Ballèvre et al. 2013). However, in the
708 Massif Central, intra-continental basins locally filled by bituminous shales, were proposed as
709 the source of reduced fluids that caused U to precipitate (Turpin et al. 1990; Marignac and
710 Cuney 1999). These Permian basins, that formed during a major episode of extension affecting
711 all western Europe (Kroner and Romer 2013), have a dominant half-graben structural style with

712 a common transtensional character (McCann et al. 1990) attesting for the role of detachments
713 and strike-slip faults in the control of the sedimentation, as illustrated in Figure 14.

714 Around 300 Ma, convective fluid infiltration in the Armorican Massif was enhanced by heat
715 from a regional late crustal magmatism event as shown by the emplacement of the late
716 equigranular leucogranite in the Pontivy-Rostrenen district (304.7 ± 2.7 Ma; Ballouard et al.
717 2017b) and leucogranitic dykes in the Guérande area (302.5 ± 2.0 Ma; Ballouard et al. 2015,
718 2017a). The Permian period in the EVB is marked by an abnormal heat flux in the crust and the
719 mantle, as illustrated, for example, by important granitic magmatism in Cornwall (Chen et al.
720 1993), in Iberia (Gutiérrez-Alonso et al. 2011) and in Central Europe (Finger, 1997; Romer et
721 al. 2007). This heat flux combined with the high heat producing character of the granites
722 enriched in radioactive elements (Vigneresse et al. 1989) likely sustained an elevated
723 geothermal gradient in the upper crust, able to enhance convective fluid flow (Scaillet et al.
724 1996). In the Guérande and Pontivy district, apatite fission tracks dating suggests that
725 leucogranite was at a temperature above 120°C, or at a depth above 4 km for a geothermal
726 gradient of 30°C/km, during the formation of the deposits (Fig. 14) (Ballouard, 2016; Ballouard
727 et al. 2017a).

728 Finally, a last U mineralizing or remobilization event occurred at ca. 220 Ma in the Pontivy-
729 Rostrenen district (Rosglas deposit; Figs. 3 and 5d). This mineralizing event is sub-
730 contemporaneous with the emplacement of microgabbro dikes in the western part of the
731 Armorican Massif between 210 and 195 Ma which marks the first step of Atlantic rifting
732 (Caroff et al. 1995; Ballèvre et al. 2013). This tectonic event likely caused fluid flow responsible
733 for late, discrete, U mobilization. Triassic and Lower Jurassic U mineralizing or mobilization
734 events are also recorded in the Mortagne district (ca. 200 Ma) and the Massif Central (ca. 210
735 – 170 Ma), and have been attributed to the tectonic movements at the origin of the opening of
736 the Tethys (Cathelineau et al. 1990; Cathelineau et al. 2012).

Conclusion

In the Late Carboniferous Pontivy-Rostrenen composite intrusion, intragranitic hydrothermal U mineralization is associated with the emplacement of peraluminous leucogranite. Mineralization is hosted in quartz veins associated with brittle structures related to strike-slip deformation along the SASZ. Our study of the U deposits and their magmatic country-rocks leads to the following conclusions:

(1) In the peraluminous monzogranite and metaluminous quartz monzodiorite samples, low U contents (< 9 ppm) and elevated Th/U values (> 3) suggest that most of their U is hosted in refractory minerals such as zircon and monazite for the former and zircon, titanite and allanite for the latter. For the peraluminous leucogranite, the highly variable U contents (~3 – 27 ppm) and Th/U ratios (~0.1 to 5) suggest that, in some samples, crystallization of magmatic uranium oxide followed by uranium oxide leaching during subsequent hydrothermal alteration and weathering occurred.

(2) Apatite is a powerful tool both for dating and tracing fluids in the system. Apatite grains from the monzogranite and quartz monzodiorite samples are unzoned or display regular zonation in CL images suggesting that these crystals kept their magmatic signature. Apatite U-Pb dating of these samples yield ages around 315 Ma which can be interpreted as emplacement or cooling ages. Apatite grains from leucogranite or episyenites samples display irregular zoning in CL (or BSE) images attributed to the mobility of Fe and Mn or As during an oxidized hydrothermal event involving surface-derived fluids. Apatite U-Pb dating of episyenite and leucogranite samples yield ages from ca. 290 to 275 Ma, interpreted to date the oxidized hydrothermal event. In the leucogranite facies associated with U deposits, the younger apatite grains are enriched in U compared to older ones, suggesting that these oxidized fluids were involved in the formation of U deposits.

(3) U-Pb dating of uranium oxide from the U deposits revealed a main Permian U mineralizing phase from 300 to 270 Ma synchronous with the oxidized hydrothermal event recorded by apatite grains from leucogranite. A late U mineralization or remobilization event also occurred during the Triassic at ca. 220 Ma.

On a regional scale, U deposition from 300 to 270 Ma in the Pontivy-Rostrenen complex is contemporaneous with the main U mineralizing phase in the Armorican Massif and the European Variscan belt. During this period, late brittle dextral deformation along the SASZ was synchronous with discrete extension in the South Armorican Domain suggesting a continuum of the ductile deformation which occurred in the region during Late Carboniferous from ca. 315 to 300 Ma. Detachment zones and regional scale strike-slip faults acted as major channels for oxidized surface-derived fluids which were in turn able to dissolve magmatic uranium oxide from fertile peraluminous leucogranite and then form hydrothermal U deposits due to the interaction with reducing lithologies and/or crustal basin derived fluids.

Acknowledgment

This study was supported by 2012-2013 NEEDS-CNRS and 2015-CESSUR-INSU (CNRS) research grants attributed to M. Poujol. We want to thank AREVA (in particular D. Virlogeux, J.M. Vergeau and P.C. Guiollard) for providing uranium oxide samples, historical reports and data and for fruitful discussions. We are grateful to Y. Lepagnot (Geosciences, Rennnes) for crushing the samples. Many thanks to J. Langlade (IFREMER, Brest), O. Rouer, S. Matthieu and L. Salsi (SCMEM - Géoressources, Nancy) for their technical supports during EPMA and SEM analyses. Thank you to N. Bouden (CRPG, Nancy) for the help during SIMS analyses. J.M., M.C. and M.C. would also like to thank AREVA for the permission to publish the present manuscript. This manuscript benefited from the comments of R. Shail and an anonymous reviewer. We want to thank R.L. Romer and G. Beaudoin for editorial handling.

References

Alabosi M (1984) Les altérations hydrothermales associées aux gisements d'uranium de Ty Gallen, Poulprio et Prat Mérien (massif de Pontivy, Morbihan, France). Dissertation, INPL (Institut National Polytechnique de Lorraine), Nancy

Ballèvre M. (2016) Une histoire géologique du Massif armoricain. Géochronique 140

Ballèvre M, Martínez Catalán JR, López-Carmona A, Pitra P, Abati J, Díez Fernández R, Ducassou C, Arenas R, Bosse V, Castiñeiras P, Fernández-Suárez J, Gómez Barreiro J, Paquette JL, Peucat, JJ, Poujol M, Ruffet G, Sánchez Martínez S (2014) Correlation of the nappe stack in the Ibero-Armorican arc across the Bay of Biscay: a joint French–Spanish project. Geol Soc Lond Spec Publ 405: 77–113. doi:10.1144/SP405.13

Ballèvre M, Bosse V, Dabard MP, Ducassou C, Fourcade S, Paquette JL, Peucat JJ, Pitra P (2013) Histoire Géologique du massif Armoricain : Actualité de la recherche. Bull Soc Geol Mineral Bretagne (D) 10-11: 5–96

Ballèvre M, Bosse V, Ducassou C, Pitra P (2009) Palaeozoic history of the Armorican Massif: Models for the tectonic evolution of the suture zones. Comptes Rendus Geosci 341: 174–201. doi:10.1016/j.crte.2008.11.009

Ballouard C (2016) Origine, évolution et exhumation des leucogranites peralumineux de la chaîne hercynienne armoricaine : implication sur la métallogénie de l'uranium, Dissertation, Université de Rennes 1. tel.archives-ouvertes.fr/tel-01434903/

Ballouard C, Poujol M, Boulvais P, Zeh A (2017b) Crustal recycling and juvenile addition during lithospheric wrenching: The Pontivy-Rostrenen magmatic complex, Armorican Massif (France), Variscan belt. Gondwana Res. 49: 222–247. doi:10.1016/j.gr.2017.06.002

Ballouard C, Poujol M, Boulvais P, Mercadier J, Tartèse R, Venneman T, Deloule E, Jolivet M, Kéré I, Cathelineau M, Cuney M (2017a) Magmatic and hydrothermal behavior of uranium in syntectonic leucogranites: The uranium mineralization associated with the Hercynian Guérande granite (Armorican Massif, France). Ore Geol Rev 80: 309–331. doi:10.1016/j.oregeorev.2016.06.034

Ballouard C, Boulvais P, Poujol M, Gapais D, Yamato P, Tartèse R, Cuney M (2015) Tectonic record, magmatic history and hydrothermal alteration in the Hercynian Guérande leucogranite, Armorican Massif, France. Lithos 220–223 : 1–22. doi:10.1016/j.lithos.2015.01.027

Béchennec F, Thiéblemont D, Audru JC (2006) Plouay 348, Carte Géologique de France 1:50 000. BRGM

Béchennec F, Thiéblemont D (2009) Bubry 349, Carte Géologique de France 1:50 000. BRGM

Berthé D, Choukroune P, Jegouzo P (1979) Orthogneiss, mylonite and non-coaxial deformation of granites: the example of the South Armorican Shear Zone. J Struct Geol 1, 31–42. doi:10.1016/0191-8141(79)90019-1

Blanc P, Baumer A, Cesbron F, Ohnenstetter D, Panczer G, Rémond G (2000) Systematic cathodoluminescence spectral analysis of synthetic doped minerals: anhydrite, apatite, calcite, fluorite, scheelite and Zircon. In: Pagel M, Barbin V, Blanc, P, Ohnenstetter D (Eds) Cathodoluminescence in geosciences, Springer, pp 127-160

Bos P, Castaing C, Clément JP, Chantraine J, Lemeille F (1997) Rostrenen 312, Carte Géologique de France 1:50 000. BRGM

Bosse V, Féraud G, Ballèvre M, Peucat JJ, Corsini M (2005) Rb–Sr and $^{40}Ar/^{39}Ar$ ages in blueschists from the Ile de Groix (Armorican Massif, France): Implications for closure mechanisms in isotopic systems. Chem Geol 220: 21–45. doi:10.1016/j.chemgeo.2005.02.019

Brown M (2010) The spatial and temporal patterning of the deep crust and implications for the process of melt extraction. Philos T Roy Soc A 368: 11-51

Brun JP, Guennoc P, Truffert C, Vairon J (2001) Cadomian tectonics in northern Brittany: a contribution of 3-D crustal-scale modelling. Tectonophysics 331: 229–246. doi:10.1016/S0040-1951(00)00244-4

Capdevila R (2010) Les granites varisques du Massif Armoricain. Bull Soc Geol Mineral Bretagne 7: 1-52

Cao S, Neubauer F (2016) Deep crustal expressions of exhumed strike-slip fault systems: Shear zone initiation on rheological boundaries. Earth-Sci Rev 162: 155–176. doi:10.1016/j.earscirev.2016.09.010

841 Carignan J, Hild P, Mevelle G, Morel J, Yeghicheyan D (2001) Routine Analyses of Trace Elements
842 in Geological Samples using Flow Injection and Low Pressure On-Line Liquid
843 Chromatography Coupled to ICP-MS: A Study of Geochemical Reference Materials BR, DR-
844 N, UB-N, AN-G and GH. Geostandards Newslett 25: 187–198. doi:10.1111/j.1751-
845 908X.2001.tb00595.x
846 Caroff M, Bellon H, Chauris L, Carron JP, Chevrier S, Gardinier A, Cotten J, Moan YL, Neidhart Y,
847 1995. Magmatisme fissural triasico-liasique dans l'ouest du Massif armoricain (France):
848 pétrologie, géochimie, âge, et modalités de la mise en place: Can J Earth Sci 32, 1921–1936.
849 doi:10.1139/e95-147
850 Cathelineau M (1981) Les Gisements Uraniferes de la Presqu'ile Guerandaise (Sud Bretagne);
851 Approche Structurale et Metallogenique. Miner Deposita 16: 227–240.
852 doi:10.1007/BF00202737
853 Cathelineau M, Boiron MC, Fourcade S, Ruffet G, Clauer N, Belcourt O, Coulibaly Y, Banks DA,
854 Guillocheau F (2012) A major Late Jurassic fluid event at the basin/basement unconformity in
855 western France: $^{40}Ar/^{39}Ar$ and K–Ar dating, fluid chemistry, and related geodynamic context.
856 Chem Geol 322–323: 99–120. doi:10.1016/j.chemgeo.2012.06.008
857 Cathelineau M, Boiron MC, Holliger P, Poty B (1990) Metallogenesis of the French part of the
858 Variscan orogen. Part II: Time-space relationships between U, Au and Sn-W ore deposition
859 and geodynamic events - mineralogical and U-Pb data. Tectonophysics 177: 59–79.
860 doi:10.1016/0040-1951(90)90274-C
861 Cháb J, Stráník Z, Eliáš M (2007) Geologická mapa České republiky 1:500 000. Česká geologická
862 služba, Praha, Czech Republic
863 Chantraine J, Autran A, Cavelier C (2003) Carte géologique de France 1:1 000 000 6ème édition
864 révisée. BRGM
865 Chauris L (1984) Accidents linéamentaires et minéralisations uranifères; L'exemple de la ceinture
866 batholitique hercynienne médio-armoricaine (France). Bull Soc Geol Fr S7–XXVI: 1375–
867 1380. doi:10.2113/gssgfbull.S7-XXVI.6.1375

868 Chen Y, Clark AH, Farrar E, Wasteneys HAHP, Hodgson MJ, Bromley AV (1993) Diachronous and
869 independent histories of plutonism and mineralization in the Cornubian Batholith, southwest
870 England. J Geol Soc 150: 1183–1191. doi:10.1144/gsjgs.150.6.1183
871 Civis Llovera J (2015) Mapas geológicos de espana y Portugal 1:1 000 000. IGME: Instituto
872 Geológico y Minero de España
873 Cotten J (1975) Etude des mégacristaux du granite de Rostrenen (Massif Armoricain). Dissertation,
874 Université de Bretagne Occidentale, Brest
875 Cuney M (2014) Felsic magmatism and uranium deposits. Bull Soc Geol Fr 185: 75–92.
876 doi:10.2113/gssgfbull.185.2.75
877 Cuney M (2006) Excursion « granites varisques et minéralisations uranifères ». L'exemple des
878 masssifs de Ploumanac'h et de Pontivy. Partie II: Métallogenèse de l'uranium. Séminaire
879 AREVA-BUM-DEX
880 Cuney M, Kyser TK (2008) Recent and not-so-recent developments in uranium deposits and
881 implications for exploration. Mineral Assoc Canada Short Course Series 39
882 Cuney M, Friedrich M, Blumenfeld P, Bourguignon A, Boiron, MC, Vigneresse JL, Poty B (1990)
883 Metallogenesis in the French part of the Variscan orogen. Part I: U preconcentrations in pre-
884 Variscan and Variscan formations - a comparison with Sn, W and Au. Tectonophysics 177:
885 39–57. doi:10.1016/0040-1951(90)90273-B
886 D'Lemos RS, Brown M, Strachan RA (1992) Granite magma generation, ascent and emplacement
887 within a transpressional orogen. J Geol Soc 149: 487–490. doi:10.1144/gsjgs.149.4.0487
888 Dadet P, Bos P, Chantraine J, Laville P, Sagon JP (1988) Pontivy 313, Carte Géologique de France
889 1:50 000. BRGM
890 Debon F, Le Fort P (1988) A cationic classification of common plutonic rocks and their magmatic
891 associations: principles, method, applications. Bull Mineral 111 (5): 493–510
892 De Saint Blanquat M, Tikoff B, Teyssier C, Vigneresse JL (1998) Transpressional kinematics and
893 magmatic arcs. Geol Soc Lond Spec Publ 135: 327–340. doi:10.1144/GSL.SP.1998.135.01.21

894 Dolníček Z, René M, Hermannová S, Prochaska W (2013) Origin of the Okrouhlá Radouň episyenite-
895 hosted uranium deposit, Bohemian Massif, Czech Republic: fluid inclusion and stable isotope
896 constraints. Miner Deposita 49: 409–425. doi:10.1007/s00126-013-0500-5
897 Dubessy J, Ramboz C, Nguyen Trung C, Cathelineau M, Charoy B, Cuney M, Leroy J, Poty B,
898 Weisbrod A (1987) Physical and chemical control (pO_2, T, pH) of the opposite behaviour of U
899 and Sn-W as exemplified by hydrothermal deposits in France and Great Britain, and solubility
900 data. Bull Mineral 110: 262–281
901 Euzen T (1993) Pétrogenèse des granites de collision post-épaississement. Le cas des granites crustaux
902 et mantelliques du complexe de Pontivy-Rostrenen (Massif Armoricain, France). Memoires
903 Géosciences Rennes 51
904 Finger F, Roberts MP, Haunschmid B, Schermaier A, Steyrer HP (1997) Variscan granitoids of central
905 Europe: their typology, potential sources and tectonothermal relations. Mineral. Petrol. 61 :
906 67–96. doi:10.1007/BF01172478
907 Förster HJ (1999) The chemical composition of uraninite in Variscan granites of the Erzgebirge,
908 Germany. Mineral Mag 63: 239–252. doi:10.1180/002646199548466
909 Förster H J, Rhede D, Hecht L (2008) Chemical composition of radioactive accessory minerals:
910 implications for the evolution, alteration, age, and uranium fertility of the Fichtelgebirge
911 granites (NE Bavaria, Germany). Neues Jahrb Fr Mineral - Abh J Mineral Geoche 185: 161–
912 182. doi:10.1127/0077-7757/2008/0117
913 Friedrich M, Cuney M, Poty B (1987) Uranium geochemistry in peraluminous leucogranites. Uranium
914 3: 353–385
915 Gaafar I (2015) Application of gamma ray spectrometric measurements and VLF-EM data for tracing
916 vein type uranium mineralization, El-Sela area, South Eastern Desert, Egypt. NRIAG J Astron
917 Geophys 4: 266–282. doi:10.1016/j.nrjag.2015.10.001
918 Gaafar I, Cuney M, Gawad AA (2014) Mineral Chemistry of Two-Mica Granite Rare Metals: Impact
919 of Geophysics on the Distribution of Uranium Mineralization at El Sela Shear Zone, Egypt.
920 Open J Geol 4: 137–160. doi:10.4236/ojg.2014.44011

921 Gapais D (1989) Shear structures within deformed granites: Mechanical and thermal indicators.
922 Geology 17: 1144–1147. doi:10.1130/0091-7613(1989)017<1144:SSWDGM>2.3.CO;2
923 Gapais D, Brun JP, Gumiaux C, Cagnard F, Ruffet G, Le Carlier De Veslud C (2015) Extensional
924 tectonics in the Hercynian Armorican belt (France). An overview. Bull Soc Geol Fr 186: 117–
925 129. doi:10.2113/gssgfbull.186.2-3.117
926 Gapais D, Lagarde JL, Le Corre C, Audren C, Jegouzo P, Casas Sainz A, Van Den Driessche J (1993)
927 La zone de cisaillement de Quiberon: témoin d'extension de la chaine varisque en Bretagne
928 méridionale au Carbonifère. C R Acad Sci, Paris, série II 316: 1123–1129
929 Gapais D, Le Corre C (1980) Is the Hercynien belt of Brittany a major shear zone? Nature 288: 574–
930 576. doi:10.1038/288574a0
931 Gébelin A, Roger F, Brunel M (2009) Syntectonic crustal melting and high-grade metamorphism in a
932 transpressional regime, Variscan Massif Central, France. Tectonophysics 477: 229–243.
933 doi:10.1016/j.tecto.2009.03.022
934 Gumiaux C, Judenherc S, Brun JP, Gapais D, Granet M, Poupinet G (2004b) Restoration of
935 lithosphere-scale wrenching from integrated structural and tomographic data (Hercynian belt
936 of western France). Geology 32: 333–336. doi:10.1130/G20134.2
937 Gumiaux C, Gapais D, Brun JP, Chantraine J, Ruffet G (2004a). Tectonic history of the Hercynian
938 Armorican Shear belt (Brittany, France). Geodin Acta 17: 289–307. doi:10.3166/ga.17.289-
939 307
940 Gutiérrez-Alonso G., Fernández-Suárez J, Jeffries TE, Johnston ST, Pastor-Galán D, Murphy JB,
941 Franco MP, Gonzalo JC (2011) Diachronous post-orogenic magmatism within a developing
942 orocline in Iberia, European Variscides. Tectonics 30, TC5008. doi:10.1029/2010TC002845
943 Harlaux M, Romer RL, Mercadier J, Morlot C, Marignac C, Cuney M (2017) 40 Ma years of
944 hydrothermal W mineralization during the Variscan orogenic evolution of the French Massif
945 Central revealed by U-Pb dating of wolframite. Miner Deposita: 1–31. doi:10.1007/s00126-
946 017-0721-0

947 Hutton DHW, Reavy RJ (1992) Strike-slip tectonics and granite petrogenesis. Tectonics 11: 960–967.
948 doi:10.1029/92TC00336
949 IRSN (2004) Inventaire national des sites miniers d'uranium. Institut de Radioprotection et de Sureté
950 Nucléaire
951 Jégouzo P, Rossello EA (1988) La Branche Nord du Cisaillement Sud-Armoricain (France): un essai
952 d'évaluation du déplacement par l'analyse des mylonites. C R Acad Sci, Paris, Série II
953 307(17): 1825-1831
954 Jégouzo P (1980) The South Armorican Shear Zone. J Struct Geol 2: 39–47. doi:10.1016/0191-
955 8141(80)90032-2
956 Judenherc S, Granet M, Brun JP, Poupinet G (2003) The Hercynian collision in the Armorican Massif:
957 evidence of different lithospheric domains inferred from seismic tomography and anisotropy.
958 Bull Soc Geol Fr 174: 45–57
959 Kříbek B, Žák K, Dobeš P, Leichmann J, Pudilová M, René M, Scharm B, Scharmová M, Hájek A,
960 Holeczy D, Hein UF, Lehmann B (2008) The Rožná uranium deposit (Bohemian Massif,
961 Czech Republic): shear zone-hosted, late Variscan and post-Variscan hydrothermal
962 mineralization. Miner Deposita 44: 99–128. doi:10.1007/s00126-008-0188-0
963 Kroner U, Romer RL (2013) Two plates - Many subduction zones: The Variscan orogeny
964 reconsidered. Gondwana Res 24: 298–329. doi:10.1016/j.gr.2013.03.001
965 Lemarchand J, Boulvais P, Gaboriau M, Boiron MC, Tartèse R, Cokkinos M, Bonnet S, Jégouzo, P
966 (2012) Giant quartz vein formation and high-elevation meteoric fluid infiltration into the
967 South Armorican Shear Zone: geological, fluid inclusion and stable isotope evidence. J Geol
968 Soc 169: 17–27. doi:10.1144/0016-76492010-186
969 Lespinasse M, Cathelineau M (1990) Fluid percolations in a fault zone: a study of fluid inclusion
970 planes in the St Sylvestre granite, northwest Massif Central, France. Tectonophysics 184:
971 173–187. doi:10.1016/0040-1951(90)90052-A
972 Li JW, Zhou MF, Li XF, Fu ZR, Li ZJ (2002) Structural control on uranium mineralization in South
973 China: Implications for fluid flow in continental strike-slip faults. Sci China Ser Earth Sci 45:
974 851–864. doi:10.1007/BF02879519

975 Li JW, Zhou MF, Li XF, Fu ZR, Li ZJ (2001) The Hunan-Jiangxi strike-slip fault system in southern
976 China: southern termination of the Tan-Lu fault. J Geodyn 32: 333–354. doi:10.1016/S0264-
977 3707(01)00033-3
978 López-Moro FJ, Moro MC, Timón SM, Cembranos ML, Cózar J (2013) Constraints regarding gold
979 deposition in episyenites: the Permian episyenites associated with the Villalcampo Shear
980 Zone, central western Spain. Int J Earth Sci 102: 721–744. doi:10.1007/s00531-012-0844-6
981 Ludwig KR (2001) Isoplot, a geochronological toolkit for Microsoft Excel. Berkeley Geochronology
982 Center, Spec Publ 5: 75
983 Ludwig KR, Simmons KR (1992) U-Pb dating of uranium deposits in collapse breccia pipes of the
984 Grand Canyon region. Econ Geol 87: 1747–1765. doi:10.2113/gsecongeo.87.7.1747
985 Marcoux E (1982) Etude géologique et métallogénique du district plombo-zincifère de Pontivy
986 (Massif armoricain, France) : Relations avec les paragenèses stannifères et uranifères. Bull
987 BRGM (2), section II, n°1: 1-24
988 Marignac C, Cuney M (1999) Ore deposits of the French Massif Central: insight into the
989 metallogenesis of the Variscan collision belt. Miner Deposita 34 : 472–504.
990 doi:10.1007/s001260050216
991 Marshall DJ (1980) Cathodoluminescence of geological materials. Hunwin Hyman
992 Miles AJ, Graham CM, Hawkesworth CJ, Gillespie MR, Hinton RW, Bromiley GD (2014) Apatite: A
993 new redox proxy for silicic magmas? Geochim Cosmochim Acta 132: 101–119.
994 doi:10.1016/j.gca.2014.01.040
995 Mitchell RH, Xiong J, Mariano AN, Fleet ME (1997) Rare-earth-element-activated
996 cathodoluminescence in apatite. Can. Mineralogist 35: 979-998
997 Peiffert C, Nguyen-Trung C, Cuney M (1996) Uranium in granitic magmas: Part 2. Experimental
998 determination of uranium solubility and fluid-melt partition coefficients in the uranium oxide-
999 haplogranite-H_2O-NaX (X = Cl, F) system at 770°C, 2 kbar. Geochim Cosmochim Acta 60:
1000 1515–1529. doi:10.1016/0016-7037(96)00039-7
1001 Peiffert C, Cuney M, Nguyen-Trung C (1994) Uranium in granitic magmas: Part 1. Experimental
1002 determination of uranium solubility and fluid-melt partition coefficients in the uranium oxide-

haplogranite-H_2O-Na_2CO_3 system at 720–770°C, 2 kbar. Geochim Cosmochim Acta 58: 2495–2507. doi:10.1016/0016-7037(94)90026-4

Pérez Del Villar L, Moro C (1991) Las mineralizaciones intragraníticas de Uranio en el batolito de Cabeza de Ar aya (provincia de Cáceres): El Saguazal, Brechas NNE y La Zafrilla. Stud Geol Salmant 27: 85-112

Perseil EA, Blanc P, Ohnenstetter D (2000) As-bearing fluorapatite in manganiferous deposits from St. Marcel – Praborna, Val d'Aosta, Italy. Can Mineralogist 38: 101-117

Pirajno F (2010) Intracontinental strike-slip faults, associated magmatism, mineral systems and mantle dynamics: examples from NW China and Altay-Sayan (Siberia). J Geodyn 50: 325–346. doi:10.1016/j.jog.2010.01.018

Pochon A, Poujol M, Gloaguen E, Branquet Y, Cagnard F, Gumiaux C, Gapais D (2016) U-Pb LA-ICP-MS dating of apatite in mafic rocks: evidence for a major magmatic event at the Devonian- Carboniferous boundary in the Armorican Massif (France). Am Mineral 101: 2430–2442. doi: 10.2138/am-2016-5844

Roeder PL, McArthur D, Ma XP, Palmer GR, Mariano A (1987) Cathodoluminescence and microprobe study of rare-earth elements in apatite. Am Mineral 72: 801-811

Romer RL, Schneider J, Linnemann U (2010) Post-Variscan deformation and hydrothermal mineralization in Saxo-Thuringia and beyond: a geochronologic review. In: Linnemann U and Romer RL (eds) Pre-Mesozoic Geology of Saxo-Thuringia – From the Cadomian Active Margin to the Variscan Orogen. Schweizerbart, Stuttgart, pp 347-360

Romer RL, Thomas R, Stein HJ, Rhede D (2007) Dating multiply overprinted Sn-mineralized granites – examples from the Erzgebirge, Germany. Miner Deposita 42: 337-359. doi:10.1007/s00126-006-0114-2

Scaillet S, Cheilletz A, Cuney M, Farrar E, Archibald DA (1996) Cooling pattern and mineralization history of the Saint Sylvestre and western Marche leucogranite pluton, French Massif Central: I. $^{40}Ar/^{39}Ar$ isotopic constraints. Geochim Cosmochim Acta 60: 4653–4671. doi:10.1016/S0016-7037(96)00291-8

1030 Sibson RH (1990) Conditions for fault-valve behaviour. Geol Soc Lond Spec Publ 54: 15–28.
1031 doi:10.1144/GSL.SP.1990.054.01.02
1032 Sibson RH (1987) Earthquake rupturing as a mineralizing agent in hydrothermal systems. Geology 15:
1033 701–704. doi:10.1130/0091-7613(1987)15<701:ERAAMA>2.0.CO;2
1034 Stacey JS, Kramers JD (1975) Approximation of terrestrial lead isotope evolution by a two-stage
1035 model. Earth Planet Sci Lett 26: 207–221. doi:10.1016/0012-821X(75)90088-6
1036 Strong DF, Hanmer SK (1981) The leucogranites of southern Brittany; origin by faulting, frictional
1037 heating, fluid flux and fractional melting. Can Mineral 19: 163–176
1038 Tartèse R, Boulvais P (2010) Differentiation of peraluminous leucogranites “en route” to the surface.
1039 Lithos 114: 353–368. doi:10.1016/j.lithos.2009.09.011
1040 Tartèse R, Boulvais P, Poujol M, Gloaguen E, Cuney M (2013) Uranium Mobilization from the
1041 Variscan Questembert Syntectonic Granite During Fluid-Rock Interaction at Depth. Econ
1042 Geol 108: 379–386. doi:10.2113/econgeo.108.2.379
1043 Tartèse R, Boulvais P, Poujol M, Chevalier T, Paquette JL, Ireland TR, Deloule E (2012) Mylonites of
1044 the South Armorican Shear Zone: Insights for crustal-scale fluid flow and water–rock
1045 interaction processes. J Geodyn 56–57: 86–107. doi:10.1016/j.jog.2011.05.003
1046 Tartèse R, Ruffet G, Poujol M, Boulvais P, Ireland TR (2011b) Simultaneous resetting of the
1047 muscovite K-Ar and monazite U-Pb geochronometers: a story of fluids. Terra Nova 23: 390–
1048 398. doi:10.1111/j.1365-3121.2011.01024.x
1049 Tartèse R, Poujol M, Ruffet G, Boulvais P, Yamato P, Košler J (2011a) New U-Pb zircon and
1050 $^{40}Ar/^{39}Ar$ muscovite age constraints on the emplacement of the Lizio syn-tectonic granite
1051 (Armorican Massif, France). Comptes Rendus Geosci 343: 443–453.
1052 doi:10.1016/j.crte.2011.07.005
1053 Tischendorf G, Förster H J (1994) Hercynian granite magmatism and related metallogenesis in the
1054 Erzgebirge: A status report. Mineral deposits of the Erzgebirge/Krusne hory (Germany/Czech
1055 Republic). Monogr Ser Mineral Deposits 31: 5-23

1056 Turpin L, Leroy JL, Sheppard SMF (1990) Isotopic systematics (O, H, C, Sr, Nd) of superimposed
1057 barren and U-bearing hydrothermal systems in a Hercynian granite, Massif Central, France.
1058 Chem Geol 88: 85–98. doi:10.1016/0009-2541(90)90105-G
1059 Turrillot P, Augier R, Faure M (2009) The top-to-the-southeast Sarzeau shear zone and its place in the
1060 late-orogenic extensional tectonics of southern Armorica. Bull Soc Geol Fr 180: 247–261.
1061 doi:10.2113/gssgfbull.180.3.247
1062 Vigneresse JL (1999) Intrusion level of granitic massifs along the Hercynian belt: balancing the
1063 eroded crust. Tectonophysics 307: 277–295. doi:10.1016/S0040-1951(99)00104-3
1064 Vigneresse JL, Brun JP (1983) Les leucogranites armoricains marqueurs de la déformation régionale;
1065 apport de la gravimétrie. Bull Soc Geol Fr S7–XXV : 357–366. doi:10.2113/gssgfbull.S7-
1066 XXV.3.357
1067 Vigneresse JL, Cuney M, Jolivet J, Bienfait G (1989) Selective heat-producing element enrichment in
1068 a crustal segment of the mid-European Variscan chain. Tectonophysics 159 : 47–60.
1069 doi:10.1016/0040-1951(89)90169-8
1070 Wan B, Xiao W, Zhang L, Han C (2012) Iron mineralization associated with a major strike–slip shear
1071 zone: Radiometric and oxygen isotope evidence from the Mengku deposit, NW China. Ore
1072 Geol Rev 44: 136–147. doi:10.1016/j.oregeorev.2011.09.011
1073 Whitney DL, Evans BW (2010) Abbreviations for names of rock-forming minerals. Am. Mineral. 95:
1074 185–187. doi:10.2138/am.2010.3371
1075

Captions

Figure 1: Schematic representation of the west European Variscan belt representing the main terranes (Ballèvre et al. 2009, 2013, 2016) and showing the relationship between Variscan granitoids and hydrothermal U deposits (after Cuney and Kyser 2008). The granite typology is based on the 1:1,000,000 geological maps of France (Chantaine et al. 2003), Portugal and Spain (Civis Llovera, 2015) and the 1: 500,000 geological maps of Czechoslovakia (Fusán et al. 1967) and Czech Republic (Cháb et al. 2007). NASZ: north Armorican shear zone; NBSASZ: northern branch of the south Armorican shear zone; SBSASZ: southern branch of the south Armorican shear zone. NEF: Nort-sur-Erdre fault. Mineral abbreviations according to Whitney and Evans (2010).

Figure 2: (a) Schematic structural map of the Armorican Massif. (b) General geological map of the Armorican Massif identifying the different type of Carboniferous granites, according to Capdevila (2010), and the locations of the principal U deposits. The geological map is modified from Chantraine et al. (2003), Gapais et al. (2015) and Ballouard et al. (2017b). NASZ: north Armorican shear zone. SBSASZ: southern branch of the south Armorican shear zone. NBSASZ: northern branch of the south Armorican shear zone. Fe-K granites: ferro-potassic granites. Mg-K granites: magnesio-potassic granites. Mineral abbreviations according to Whitney and Evans (2010).

Figure 3: Geological map of the Pontivy-Rostrenen magmatic complex showing the different magmatic units and locations of U deposits. Sample locations from this and previous studies are shown on the map. The map is redrawn from Euzen (1993), Ballouard et al. (2017b) and from the 1: 50,000 BRGM geological maps of Pontivy (Dadet et al. 1988), Rostrenen (Bos et al. 1997), Plouay (Bechennec et al. 2006) and Bubry (Bechennec and Thiéblemont 2009). SASZ: south Armorican shear zone. The types of uranium deposits and their main orientations are from Marcoux (1982) and Cuney (2006). Qst: Quistiave; Krh: Kerroch; PM: Prat Mérrien; PP: Poulprio; Sul: Sulliado; Qsn: Quistinic; Krl: Kerlech (Lignol); Bnt: Bonote; Rsg: Rosglas; Qrn: Quérrien (Kerjean); Krs: Kerségalec. Guill.: Guilligomarch.

Figure 4: Backscattered electron images for uranium oxides (Ur) from uranium deposits of the Pontivy-Rostrenen district. (a) Pseudo-spherulitic U oxide crosscut by a fracture filled with quartz, alteration product of U oxide (Alt Ur1) and galena (Quistiave deposit). (b) Spherulitic U oxide nodule from the Kerroch deposit. The nodule that occur inside a granitic country-rock is crosscut by several veinlets filled with sulfides. (c) Vein of pseudo-spherulitic U oxides inside a granitic country rock (Undifferentiated-Guern). (d) U oxide in a quartz vein from the Kerlech deposit. The first generation of spherulutic U oxide (Ur1) was breccified by quartz and a second generation of U oxide (Ur2). (e) Cluster of U oxide spherules occurring inside a granitic country rock (Rosglas deposit). (f) U oxides from the Quérrien (Kerjean) deposit. Dark gray zones (alt Ur1) corresponds to the alteration of the first generation of U oxide. Red dashed ellipses represent the location of SIMS U-Pb analyses with the corresponding $^{207}Pb/^{206}Pb$ age. The white bar represents 100 µm.

Figure 5: Wetherill concordia diagrams displaying the analyses made on uranium oxides from the (a) Quistiave, (b) Kerroch, (c) undifferentiated-Guern, (d) Kerlech, (e) Rosglas, (f) Quérrien uranium deposits. Ellipses and age errors are reported at 2 σ.

Figure 6: Geochemical diagrams showing the whole-rock compositions of samples from the Pontivy-Rostrenen magmatic complex. (a) Q-P diagram (after Debon and Le Fort 1988) where the dashed fields delimit the location of common igneous rock: gr = granite, ad = adamellite (monzogranite), gd = granodiorite, to = tonalite, sq = quartz syenite, mzq = quartz monzonite, mzdq = quartz monzodiorite, s = syenite, mz = monzonite, mzgo = monzogabbro and go = gabbro. Q-P parameters are expressed in molar proportion multiplied by 1000. The grey arrows represent the compositional evolution of leucogranite during episyenitization. (b) U versus Th diagram where the pink arrow represents the theoretical evolution of a peraluminous leucogranitic melt during fractional crystallization and the red and green arrows represent the evolution of a sample during uranium oxide (UO_2) and monazite (Mnz)

1128 leaching, respectively. The sample compositions are from Ballouard et al. (2017b), Cotten (1975),
1129 Alabosi (1984), Euzen (1993), Bechennec et al. (2006, 2009) and Tartèse et al. (2012).

1130

1131 Figure 7: Selected images of apatite grains from magmatic and metasomatic rocks of the Pontivy-
1132 Rostrenen complex. (a) Cathodoluminescence (CL) images and chemical maps of Fe and Mn for apatite
1133 from leucogranite. (b) CL, backscattered electron (BSE) images and chemical map of As for apatite
1134 from an episyenite. (c) CL image and chemical map of Si for apatite from a monzogranite. (d) CL and
1135 BSE images for apatite from a quartz-monzodiorite. Numbers in yellow represent the associated ^{207}Pb
1136 corrected age whereas dashed circles and associated numbers represent the location of CL emission
1137 measurements (Fig. 8). The white bar represents 100 µm.

1138

1139 Figure 8: Cathodoluminescence emission spectra of representative apatite grains from (a) leucogranite,
1140 (b) episyenite, (c) monzogranite and (d) quartz monzodiorite of complex. The locations of analyses are
1141 indicated in Figure 7.

1142

1143 Figure 9: Fe versus Mn diagram displaying the EPMA analyses made on apatite grains from the
1144 granitoids of the complex. APFU = atoms per formula unit.

1145

1146 Figure 10: Tera-Wasserbug concordia diagrams with the corresponding ^{207}Pb corrected ages for LA-
1147 ICP-MS analyses made on apatite grains from (a) porphyritic leucogranite, (b-c) equigranular
1148 leucogranite, (d) late equigranular leucogranite, (e) episyenite, (f) monzogranite and (g) quartz
1149 monzodiorite of the complex. ^{207}Pb corrected ages are calculated using the common Pb composition at
1150 the lower intercept age (Stacey and Kramers 1975). Dashed ellipses in (e) represent analyses not used
1151 for ages calculations. Ellipses and errors on ages are reported at 2σ. The main period of U deposit
1152 formation in the complex is reported for comparison (green double arrow).

1153

1154 Figure 11: $^{235}U/^{207}Pb$ versus $^{206}Pb/^{207}Pb$ concordia diagram displaying the uranium oxide analyses from
1155 the uranium deposits of the complex and reporting the theoretical trajectories of uranium daughter loss
1156 (Ludwig and Simmons 1992).

1157

1158 Figure 12: Diagram reporting the U content of apatite from the granitoids of the complex as a function
1159 of the corresponding ^{207}Pb corrected age obtained by LA-ICP-MS.

1160

1161 Figure 13: Tera-Wasserbug concordia diagrams reporting LA-ICP-MS apatite analyses characterized by
1162 young ^{207}Pb corrected ages for the (a) porphyritic leucogranite, (b-c) equigranular leucogranite and (d)
1163 Late equigranular leucogranite (Fig. 10). The main period of U deposits formation in the complex is
1164 reported for comparison (grey double arrow). Ellipses and age errors are reported at 2σ.

1165

1166 Figure 14: Schematic bloc diagram summarizing the geodynamic context of U mineralization formation
1167 in the Armorican Variscan Belt from 300 to 270 Ma. A schematic cross section representing the
1168 topography at the end of the Variscan orogeny is represented in the background. NASZ: north Armorican
1169 shear zone; NBSASZ: northern branch of the south Armorican shear zone; SBSASZ: southern branch
1170 of the south Armorican shear zone; Grn: Guern; PP: Poulprio; PM: Prat Mérrien; Krl: Kerlech (Lignol);
1171 Bnt: Bonote; Mn: Métairie-Neuve; Pnr: Pen Ar Ran. See text for details.

1172

1173 Table 1: Whole-rock major and trace elements composition of episyenite samples.

1174

1175 Table 2: Average chemical composition of apatite.

1176

1177 Table 3: Comparison between the different U-Pb ages obtained on zircon (Ballouard et al. 2017b) and

1178 apatite grains from samples of the Pontivy-Rostrenen complex.

Figure 1

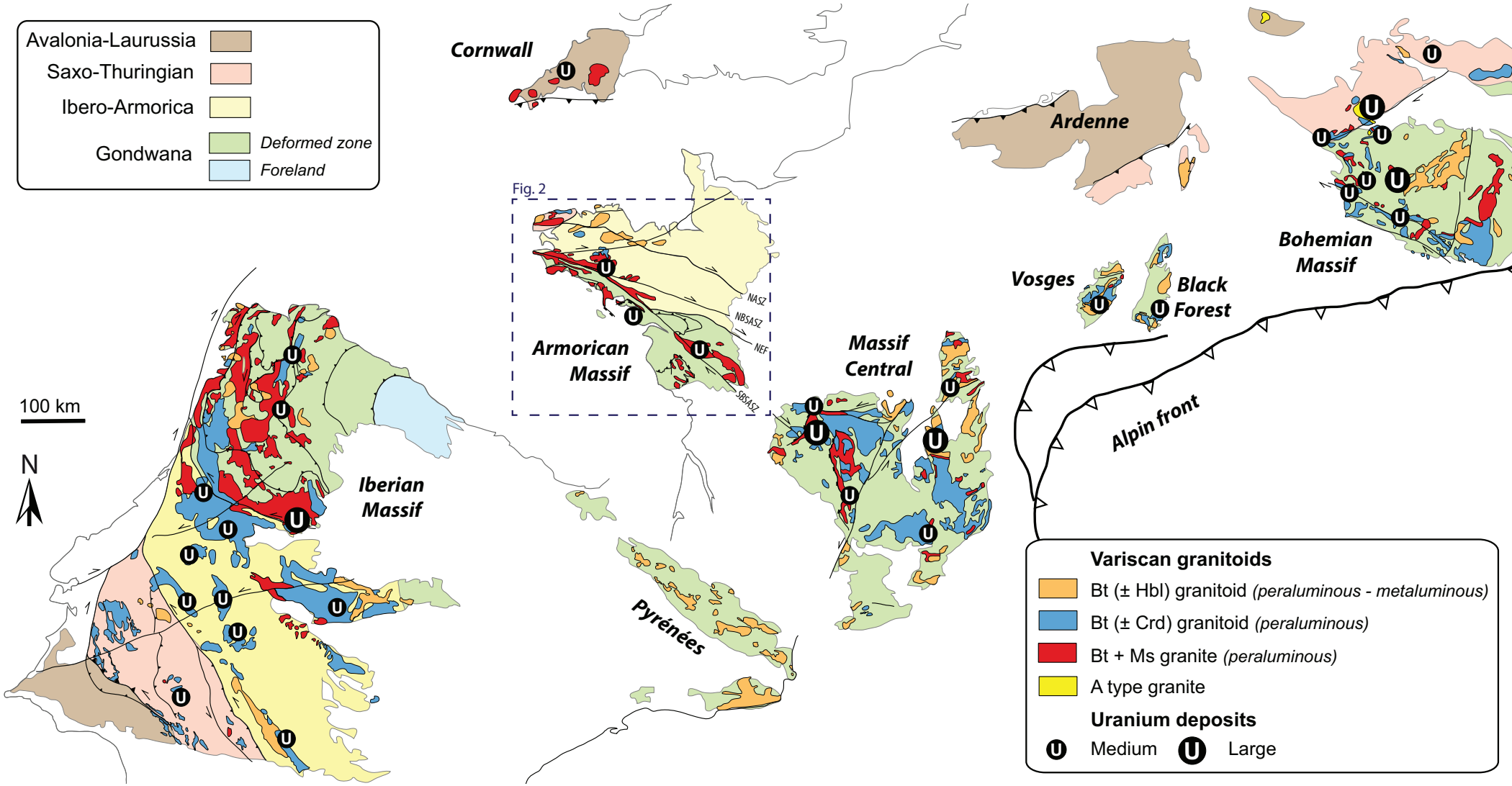
Avalonia-Laurussia
Saxo-Thuringian
Ibero-Armorica
Gondwana
Deformed zone
Foreland
Cornwall
Ardenne
Bohemian Massif
Fig. 2
NASZ
NBSASZ
NEF
SBSASZ
Armorican Massif
Massif Central
Vosges
Black Forest
Alpin front
Iberian Massif
Pyrénées
100 km
N
Variscan granitoids
Bt (± Hbl) granitoid (peraluminous - metaluminous)
Bt (± Crd) granitoid (peraluminous)
Bt + Ms granite (peraluminous)
A type granite
Uranium deposits
Medium
Large

Figure 2

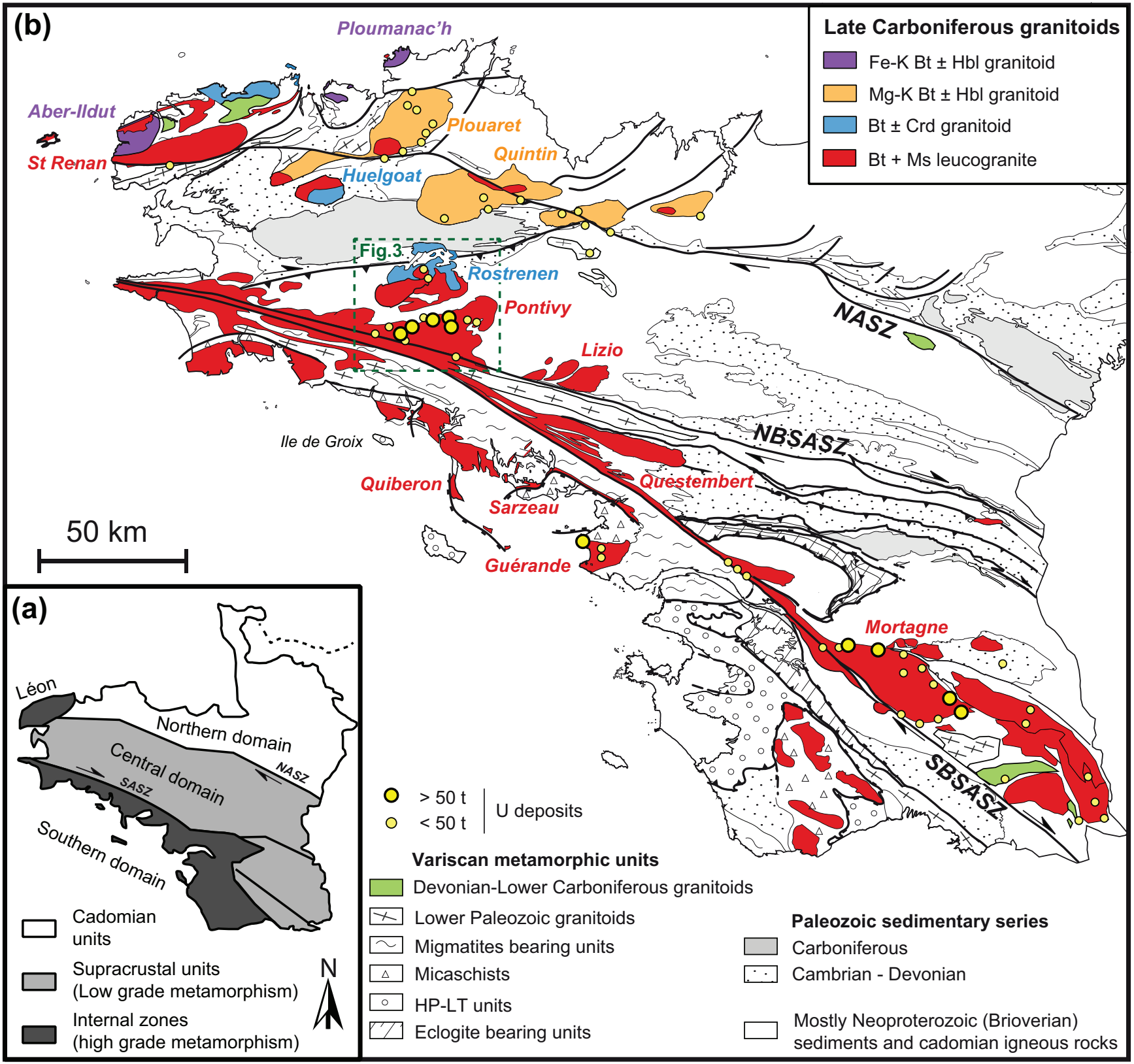
(b)
Ploumanac'h
Aber-Ildut
St Renan
Plouaret
Quintin
Huelgoat
Fig.3
Rostrenen
Pontivy
Lizio
NASZ
NBSASZ
Ile de Groix
Quiberon
Questembert
Sarzeau
Guérande
Mortagne
SBSASZ
50 km
Late Carboniferous granitoids
Fe-K Bt ± Hbl granitoid
Mg-K Bt ± Hbl granitoid
Bt ± Crd granitoid
Bt + Ms leucogranite
(a)
Léon
Northern domain
Central domain
Southern domain
NASZ
SASZ
Cadomian units
Supracrustal units (Low grade metamorphism)
Internal zones (high grade metamorphism)
N
> 50 t
< 50 t
U deposits
Variscan metamorphic units
Devonian-Lower Carboniferous granitoids
Lower Paleozoic granitoids
Migmatites bearing units
Micaschists
HP-LT units
Eclogite bearing units
Paleozoic sedimentary series
Carboniferous
Cambrian - Devonian
Mostly Neoproterozoic (Brioverian) sediments and cadomian igneous rocks

Figure 3

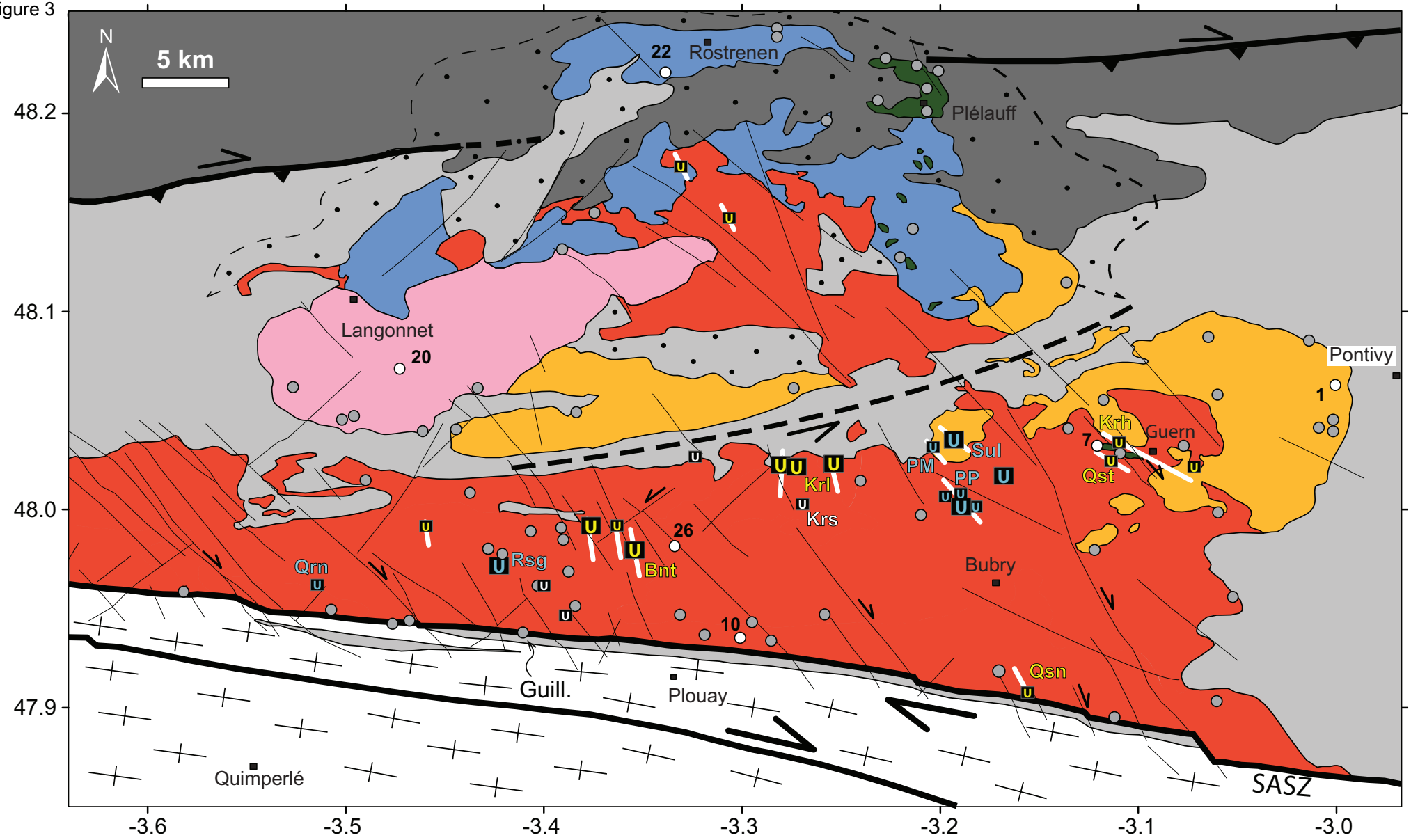

Late equigranular leucogranite (Ms ± Bt)

Equigranular leucogranite (Ms + Bt)

Porphyritic leucogranite (Ms + Bt)

Monzogranite (Bt ± Ms ± Cd)

Quartz monzodiorite (Bt - Act ± Cpx)

Orthogneiss

Paleozoic sedimentary formations

Late proterozoic sedimentary formations

Contact metamorphism

7 Sample number (this study)

Sample (previous studies)

Faults

Uranium deposits

Name	Type	Tonnage
U Qst	*Veins*	U ≥ 50 t
U PM	*Episyenite*	u < 50 t
U	*Unidentified*	
	Main orientation of the mineralization	

Figure 4

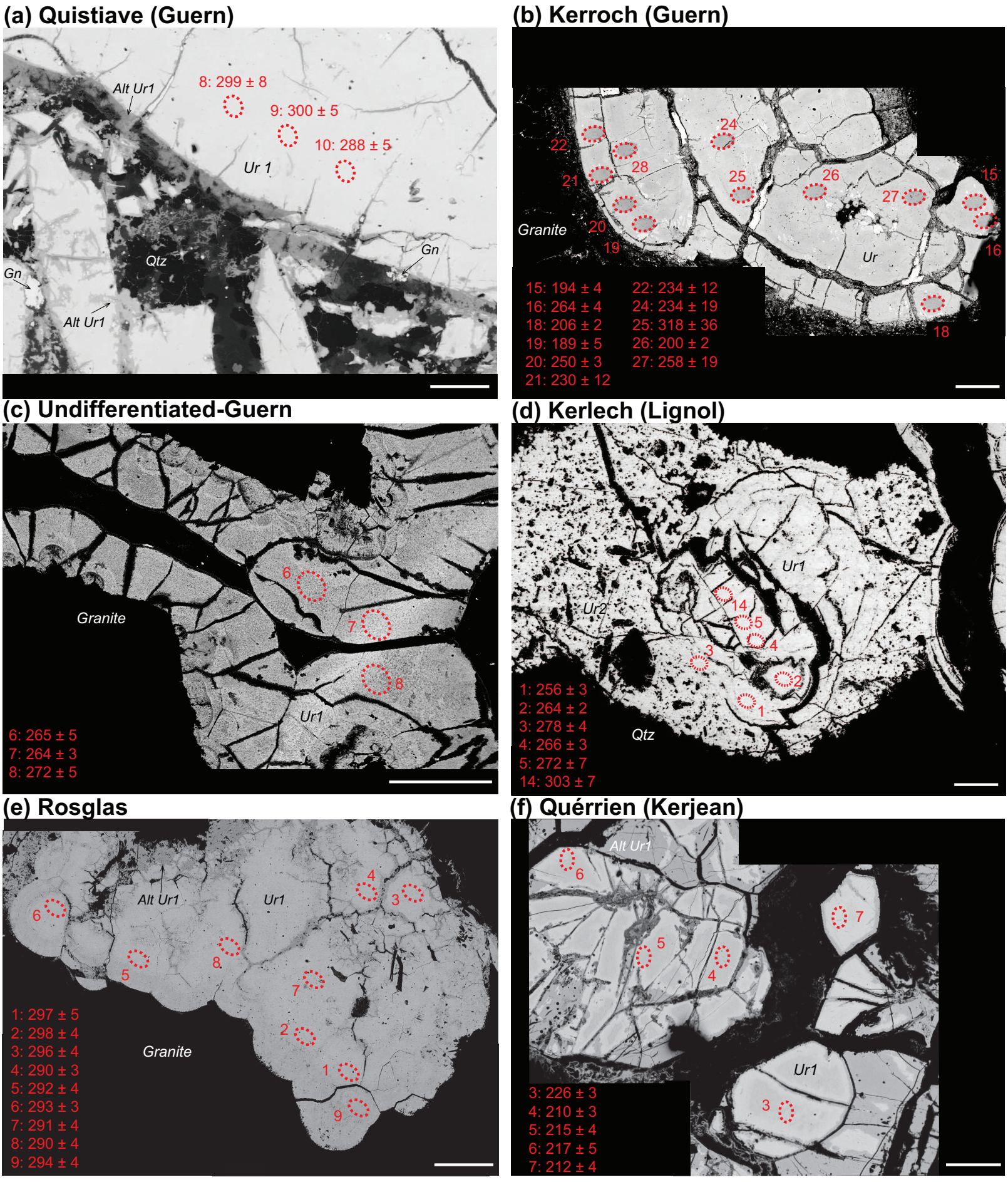
(a) Quistiave (Guern)
Alt Ur1
8: 299 ± 8
9: 300 ± 5
10: 288 ± 5
Ur 1
Qtz
Gn
Gn
Alt Ur1
(b) Kerroch (Guern)
22
24
28
21
25
26
15
27
Granite
20
19
Ur
16
18
15: 194 ± 4
16: 264 ± 4
18: 206 ± 2
19: 189 ± 5
20: 250 ± 3
21: 230 ± 12
22: 234 ± 12
24: 234 ± 19
25: 318 ± 36
26: 200 ± 2
27: 258 ± 19
(c) Undifferentiated-Guern
6
Granite
7
8
Ur1
6: 265 ± 5
7: 264 ± 3
8: 272 ± 5
(d) Kerlech (Lignol)
Ur1
Ur2
14
5
4
3
2
1
1: 256 ± 3
2: 264 ± 2
3: 278 ± 4
4: 266 ± 3
5: 272 ± 7
14: 303 ± 7
Qtz
(e) Rosglas
Alt Ur1
Ur1
6
4
3
8
5
7
2
1
9
1: 297 ± 5
2: 298 ± 4
3: 296 ± 4
4: 290 ± 3
5: 292 ± 4
6: 293 ± 3
7: 291 ± 4
8: 290 ± 4
9: 294 ± 4
Granite
(f) Quérrien (Kerjean)
Alt Ur1
6
7
5
4
Ur1
3
3: 226 ± 3
4: 210 ± 3
5: 215 ± 4
6: 217 ± 5
7: 212 ± 4

Figure 5

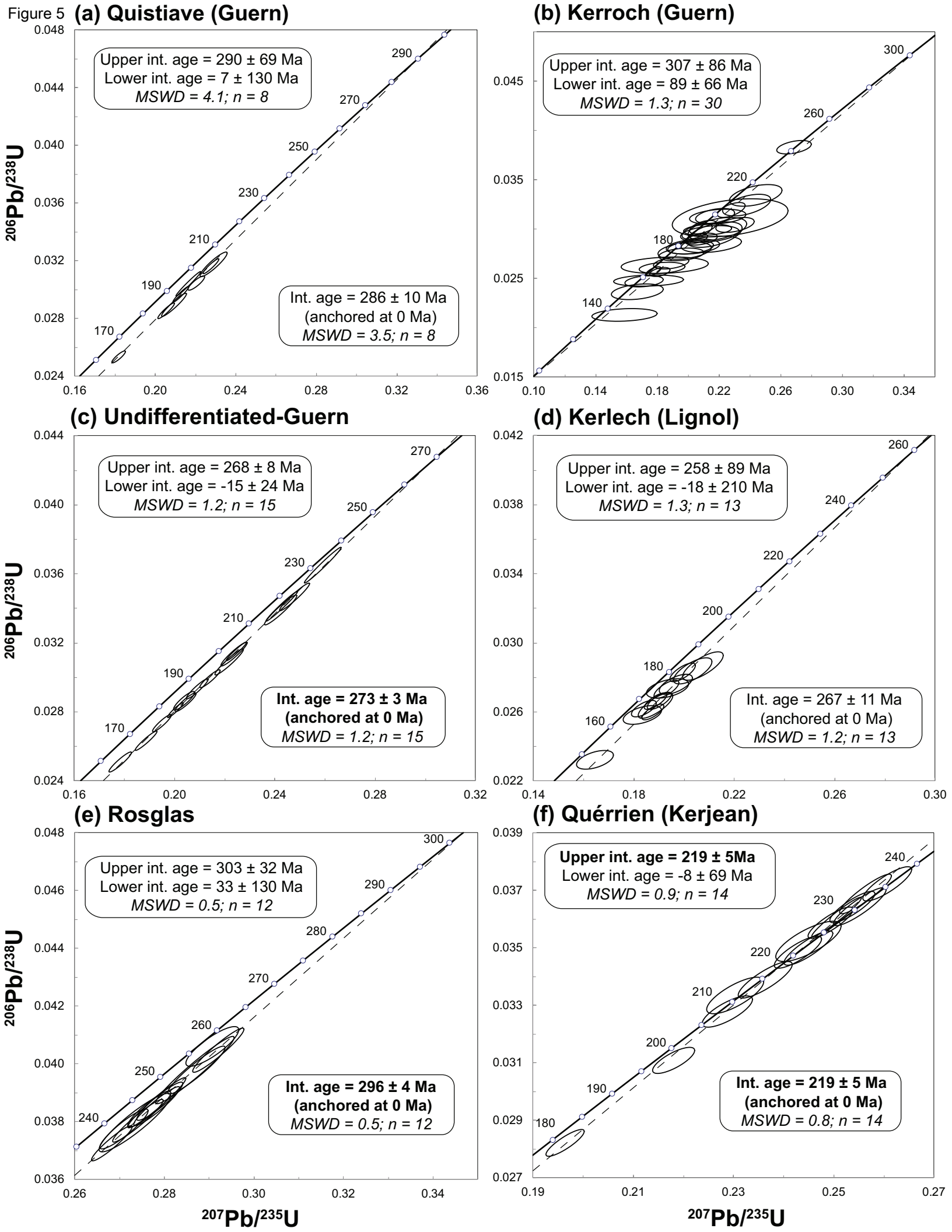
(a) Quistiave (Guern)
Upper int. age = 290 ± 69 Ma
Lower int. age = 7 ± 130 Ma
MSWD = 4.1; n = 8
Int. age = 286 ± 10 Ma
(anchored at 0 Ma)
MSWD = 3.5; n = 8
(b) Kerroch (Guern)
Upper int. age = 307 ± 86 Ma
Lower int. age = 89 ± 66 Ma
MSWD = 1.3; n = 30
(c) Undifferentiated-Guern
Upper int. age = 268 ± 8 Ma
Lower int. age = -15 ± 24 Ma
MSWD = 1.2; n = 15
Int. age = 273 ± 3 Ma
(anchored at 0 Ma)
MSWD = 1.2; n = 15
(d) Kerlech (Lignol)
Upper int. age = 258 ± 89 Ma
Lower int. age = -18 ± 210 Ma
MSWD = 1.3; n = 13
Int. age = 267 ± 11 Ma
(anchored at 0 Ma)
MSWD = 1.2; n = 13
(e) Rosglas
Upper int. age = 303 ± 32 Ma
Lower int. age = 33 ± 130 Ma
MSWD = 0.5; n = 12
Int. age = 296 ± 4 Ma
(anchored at 0 Ma)
MSWD = 0.5; n = 12
(f) Quérrien (Kerjean)
Upper int. age = 219 ± 5Ma
Lower int. age = -8 ± 69 Ma
MSWD = 0.9; n = 14
Int. age = 219 ± 5 Ma
(anchored at 0 Ma)
MSWD = 0.8; n = 14
206Pb/238U
207Pb/235U

Figure 6

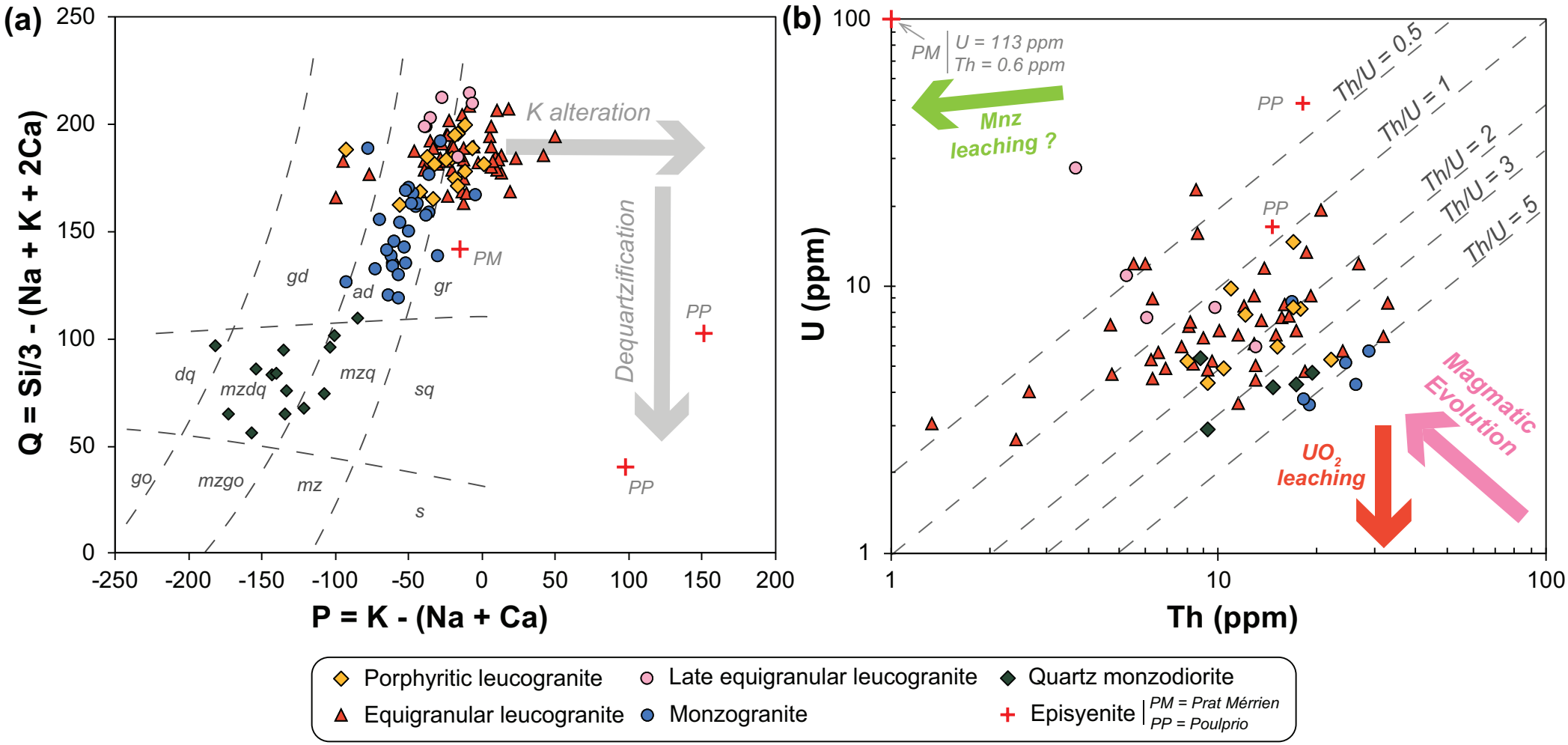
(a)
Q = Si/3 - (Na + K + 2Ca)
P = K - (Na + Ca)
K alteration
Dequartzification
PM
PP
PP
gd
ad
gr
dq
mzdq
mzq
sq
go
mzgo
mz
s
(b)
U (ppm)
Th (ppm)
PM
U = 113 ppm
Th = 0.6 ppm
Mnz
leaching ?
PP
PP
Th/U = 0.5
Th/U = 1
Th/U = 2
Th/U = 3
Th/U = 5
Magmatic
Evolution
UO2
leaching
Porphyritic leucogranite
Equigranular leucogranite
Late equigranular leucogranite
Monzogranite
Quartz monzodiorite
Episyenite
PM = Prat Mérrien
PP = Poulprio

Figure 7

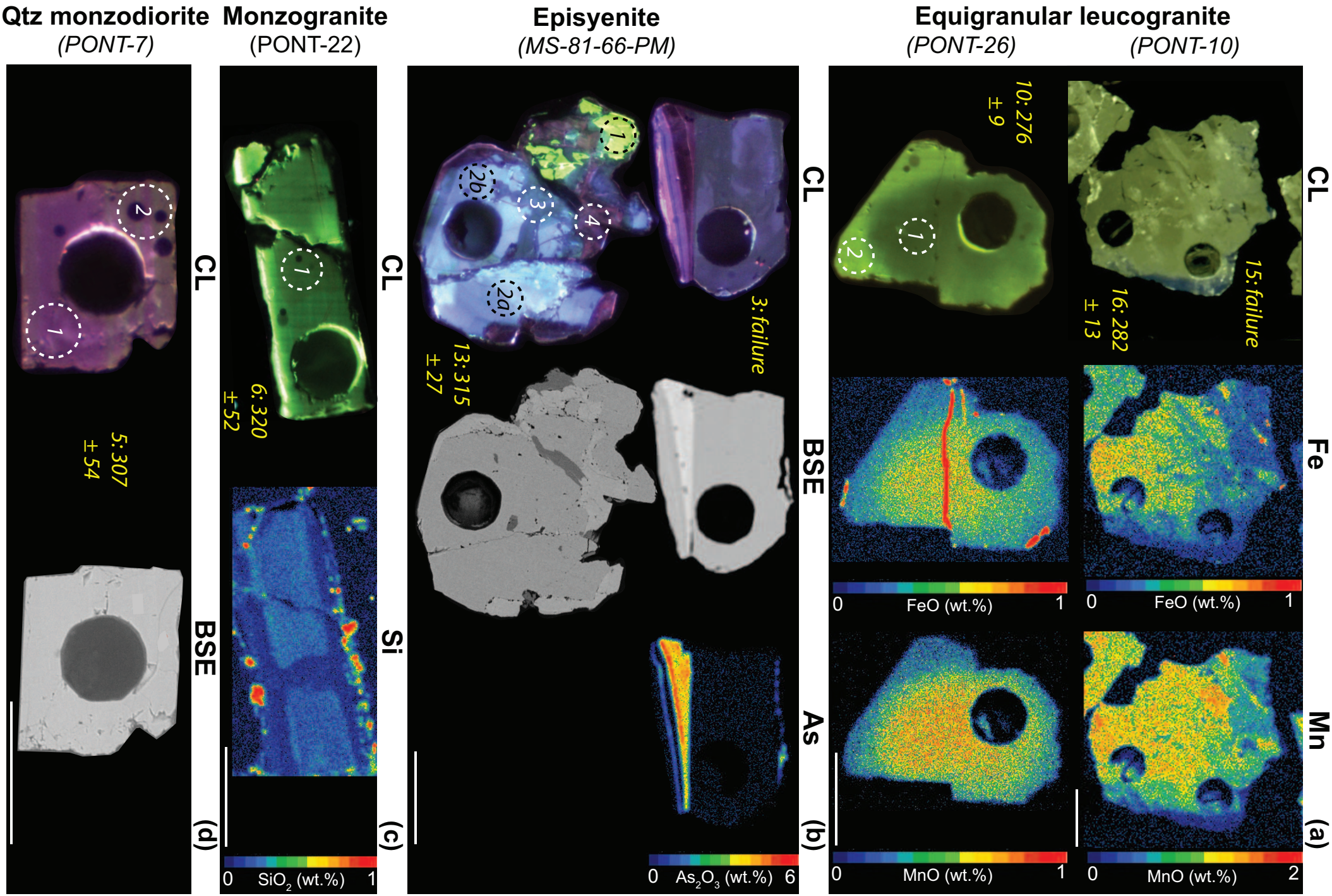
Equigranular leucogranite
(PONT-26)
(PONT-10)
Episyenite
(MS-81-66-PM)
Monzogranite
(PONT-22)
Qtz monzodiorite
(PONT-7)
CL
Fe
Mn
BSE
As
Si
(a)
(b)
(c)
(d)
15: failure
16: 282 ± 13
10: 276 ± 9
3: failure
13: 315 ± 27
6: 320 ±52
5: 307 ± 54
0 FeO (wt.%) 1
0 MnO (wt.%) 2
0 MnO (wt.%) 1
0 As2O3 (wt.%) 6
0 SiO2 (wt.%) 1

Figure 8

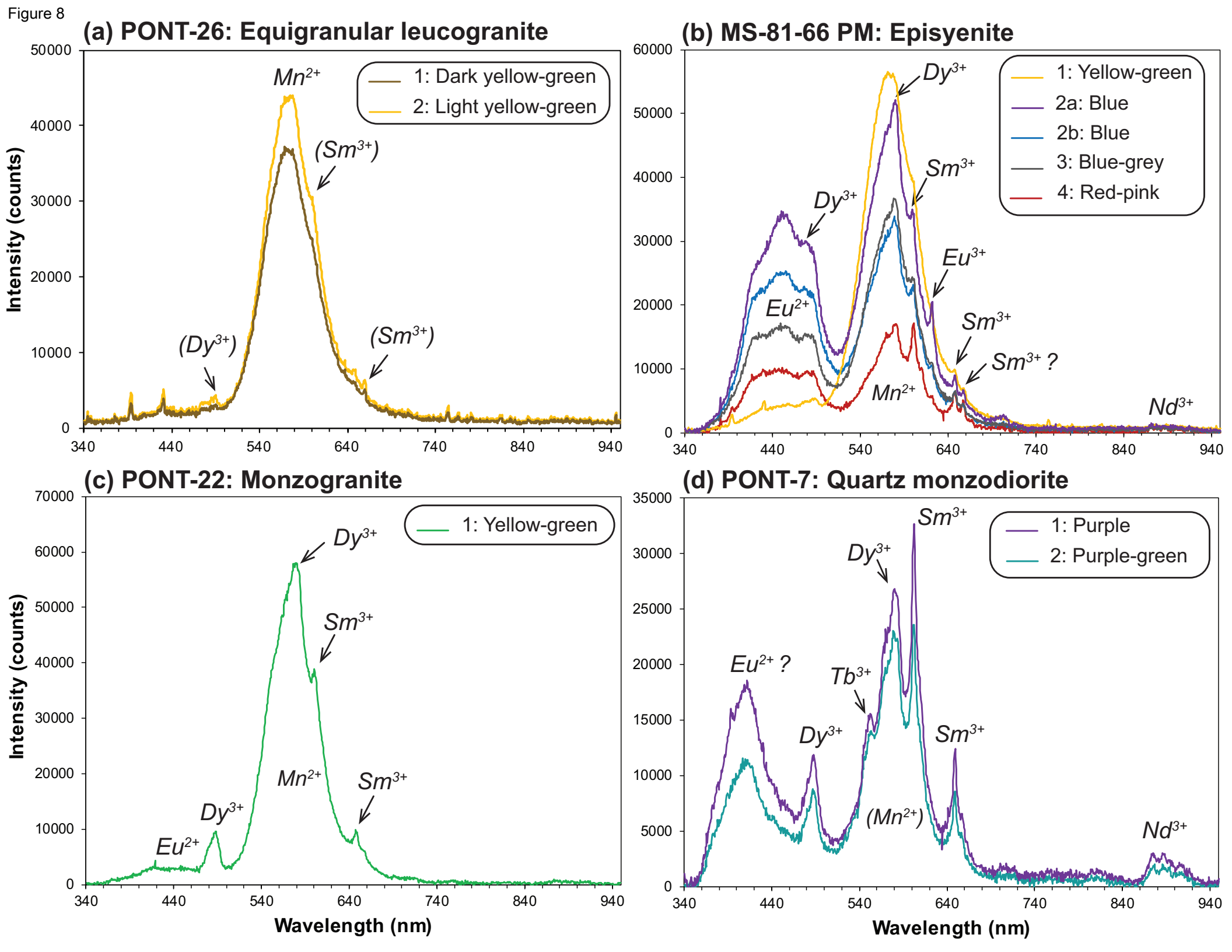
(a) PONT-26: Equigranular leucogranite
1: Dark yellow-green
2: Light yellow-green
Mn2+
(Sm3+)
(Dy3+)
(Sm3+)
Intensity (counts)
(b) MS-81-66 PM: Episyenite
1: Yellow-green
2a: Blue
2b: Blue
3: Blue-grey
4: Red-pink
Dy3+
Dy3+
Sm3+
Eu3+
Eu2+
Sm3+
Sm3+ ?
Mn2+
Nd3+
(c) PONT-22: Monzogranite
1: Yellow-green
Dy3+
Sm3+
Mn2+
Sm3+
Dy3+
Eu2+
Intensity (counts)
Wavelength (nm)
(d) PONT-7: Quartz monzodiorite
1: Purple
2: Purple-green
Sm3+
Dy3+
Eu2+ ?
Tb3+
Dy3+
Sm3+
(Mn2+)
Nd3+
Wavelength (nm)

Figure 9

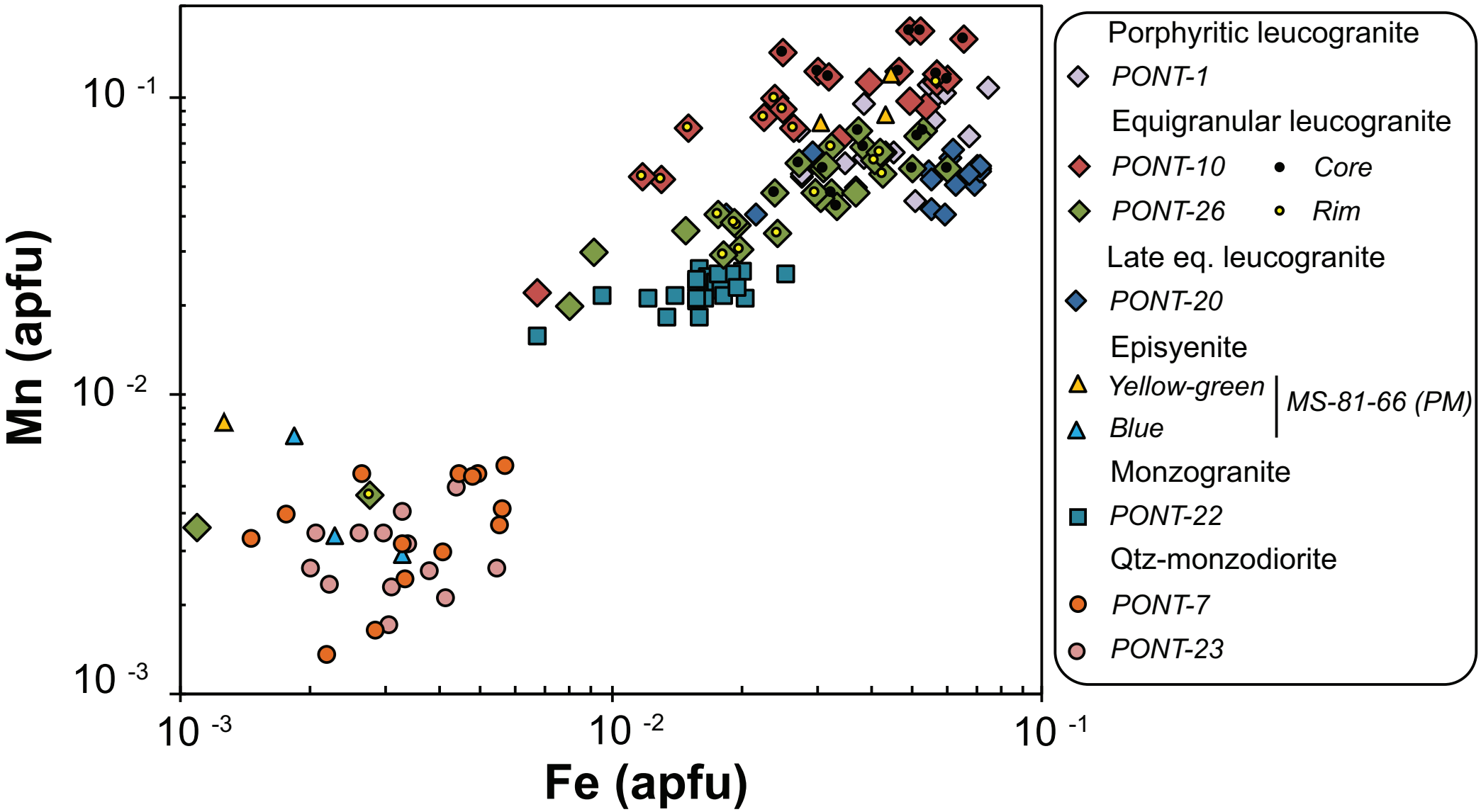
Mn (apfu)
10 -1
10 -2
10 -3
10 -3
10 -2
10 -1
Fe (apfu)
Porphyritic leucogranite
PONT-1
Equigranular leucogranite
PONT-10
PONT-26
Core
Rim
Late eq. leucogranite
PONT-20
Episyenite
Yellow-green
Blue
MS-81-66 (PM)
Monzogranite
PONT-22
Qtz-monzodiorite
PONT-7
PONT-23

Figure 10

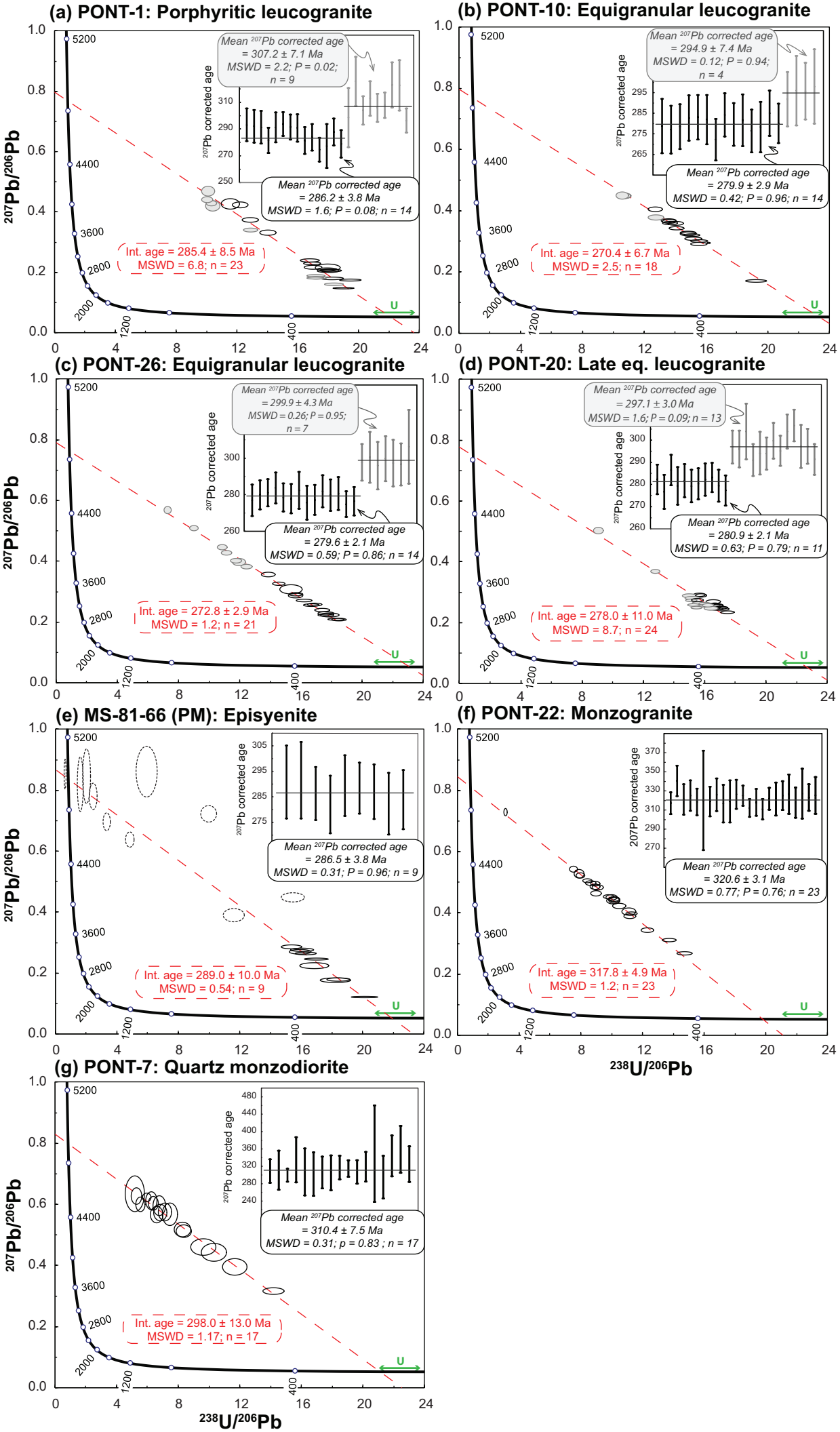
(a) PONT-1: Porphyritic leucogranite
Mean 207Pb corrected age = 307.2 ± 7.1 Ma MSWD = 2.2; P = 0.02; n = 9
Mean 207Pb corrected age = 286.2 ± 3.8 Ma MSWD = 1.6; P = 0.08; n = 14
Int. age = 285.4 ± 8.5 Ma MSWD = 6.8; n = 23
(b) PONT-10: Equigranular leucogranite
Mean 207Pb corrected age = 294.9 ± 7.4 Ma MSWD = 0.12; P = 0.94; n = 4
Mean 207Pb corrected age = 279.9 ± 2.9 Ma MSWD = 0.42; P = 0.96; n = 14
Int. age = 270.4 ± 6.7 Ma MSWD = 2.5; n = 18
(c) PONT-26: Equigranular leucogranite
Mean 207Pb corrected age = 299.9 ± 4.3 Ma MSWD = 0.26; P = 0.95; n = 7
Mean 207Pb corrected age = 279.6 ± 2.1 Ma MSWD = 0.59; P = 0.86; n = 14
Int. age = 272.8 ± 2.9 Ma MSWD = 1.2; n = 21
(d) PONT-20: Late eq. leucogranite
Mean 207Pb corrected age = 297.1 ± 3.0 Ma MSWD = 1.6; P = 0.09; n = 13
Mean 207Pb corrected age = 280.9 ± 2.1 Ma MSWD = 0.63; P = 0.79; n = 11
Int. age = 278.0 ± 11.0 Ma MSWD = 8.7; n = 24
(e) MS-81-66 (PM): Episyenite
Mean 207Pb corrected age = 286.5 ± 3.8 Ma MSWD = 0.31; P = 0.96; n = 9
Int. age = 289.0 ± 10.0 Ma MSWD = 0.54; n = 9
(f) PONT-22: Monzogranite
Mean 207Pb corrected age = 320.6 ± 3.1 Ma MSWD = 0.77; P = 0.76; n = 23
Int. age = 317.8 ± 4.9 Ma MSWD = 1.2; n = 23
(g) PONT-7: Quartz monzodiorite
Mean 207Pb corrected age = 310.4 ± 7.5 Ma MSWD = 0.31; p = 0.83 ; n = 17
Int. age = 298.0 ± 13.0 Ma MSWD = 1.17; n = 17
207Pb/206Pb
238U/206Pb
207Pb corrected age
U

Figure 11

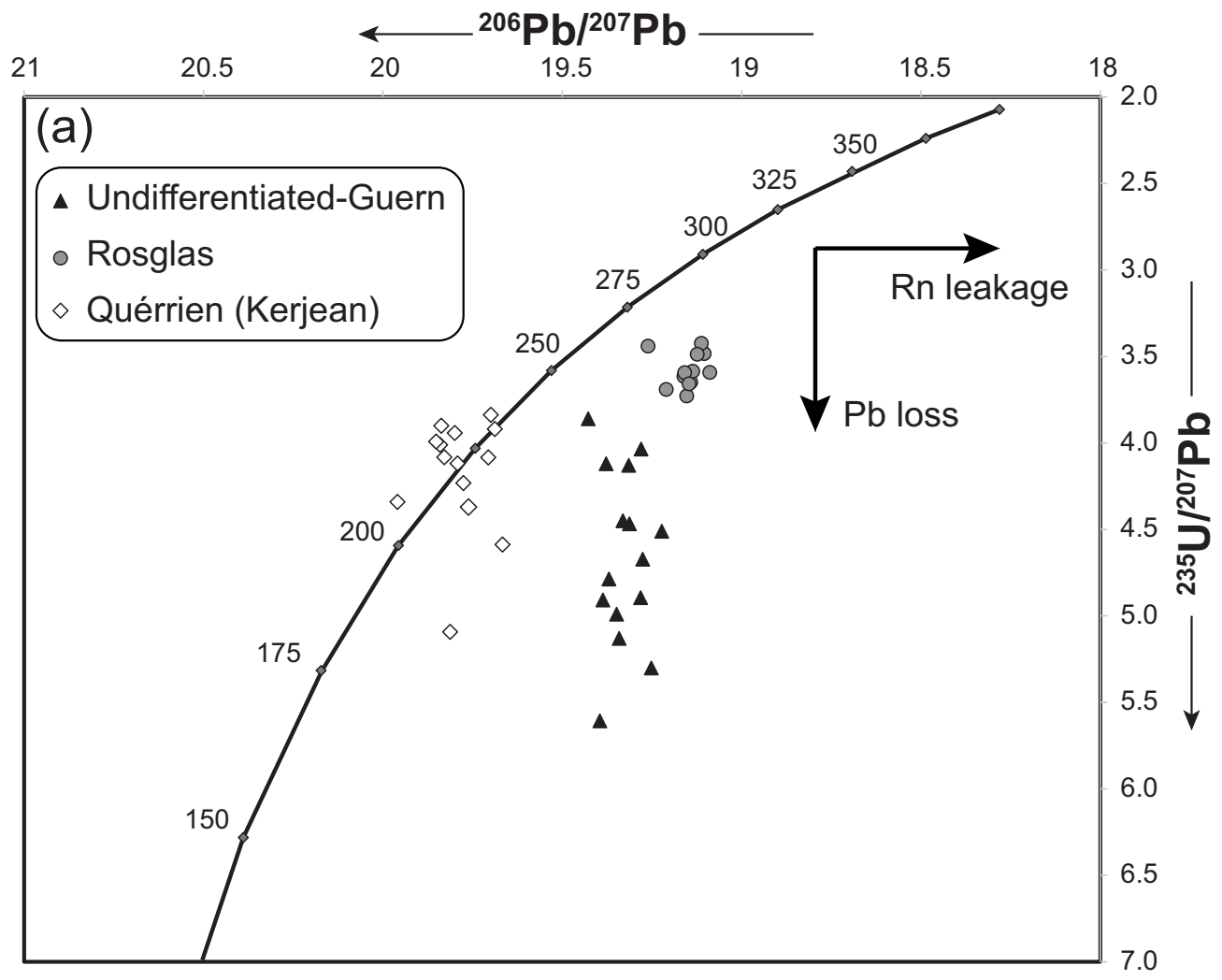
(a)
Undifferentiated-Guern
Rosglas
Quérrien (Kerjean)
Rn leakage
Pb loss
206Pb/207Pb
235U/207Pb
21
20.5
20
19.5
19
18.5
18
2.0
2.5
3.0
3.5
4.0
4.5
5.0
5.5
6.0
6.5
7.0
350
325
300
275
250
200
175
150

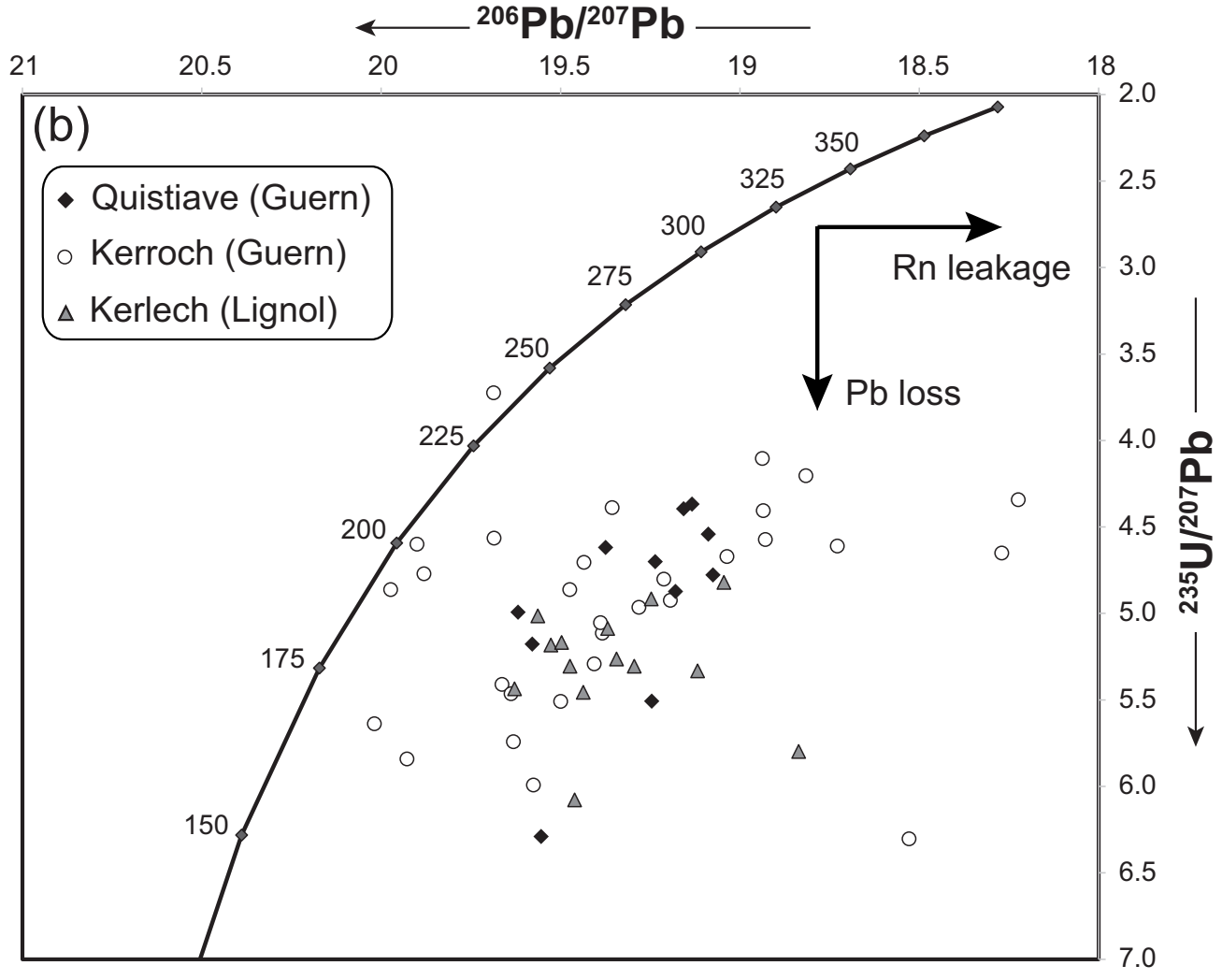
(b)
Quistiave (Guern)
Kerroch (Guern)
Kerlech (Lignol)
Rn leakage
Pb loss
206Pb/207Pb
235U/207Pb
21
20.5
20
19.5
19
18.5
18
2.0
2.5
3.0
3.5
4.0
4.5
5.0
5.5
6.0
6.5
7.0
350
325
300
275
250
225
200
175
150

Figure 12

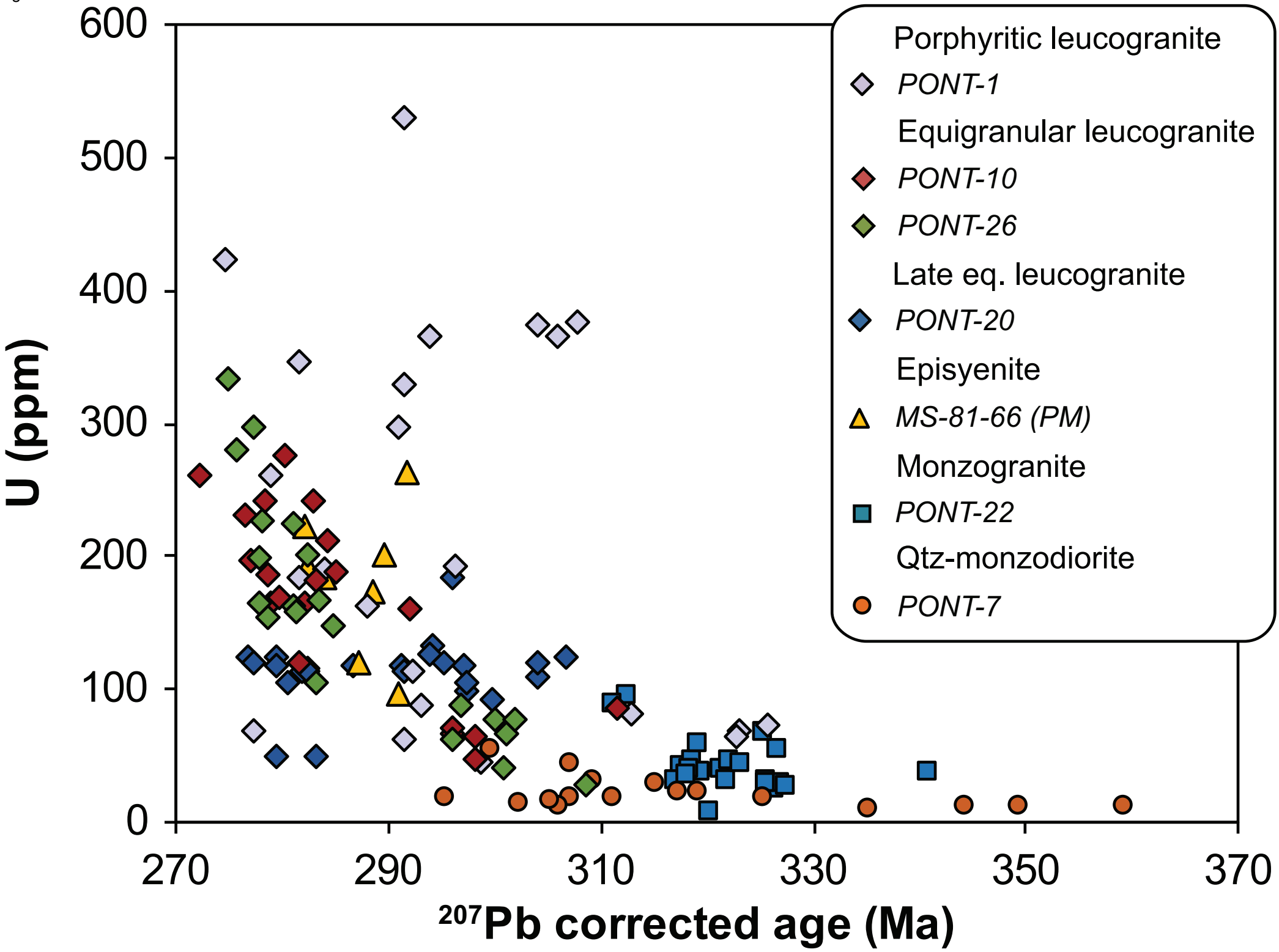
600
500
400
300
200
100
0
U (ppm)
270
290
310
330
350
370
207Pb corrected age (Ma)
Porphyritic leucogranite
PONT-1
Equigranular leucogranite
PONT-10
PONT-26
Late eq. leucogranite
PONT-20
Episyenite
MS-81-66 (PM)
Monzogranite
PONT-22
Qtz-monzodiorite
PONT-7

Figure 13

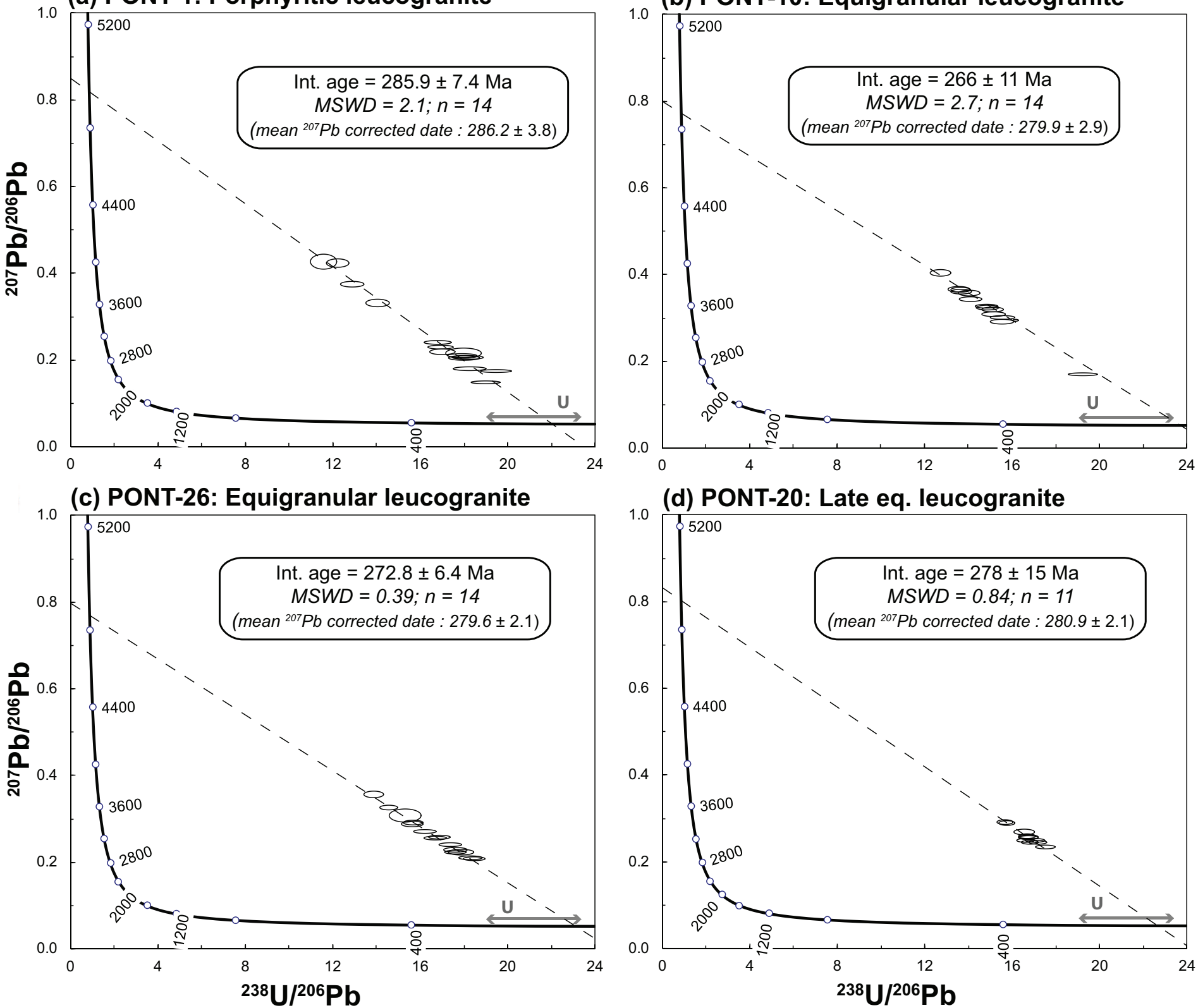
(a) PONT-1: Porphyritic leucogranite
Int. age = 285.9 ± 7.4 Ma
MSWD = 2.1; n = 14
(mean 207Pb corrected date : 286.2 ± 3.8)
(b) PONT-10: Equigranular leucogranite
Int. age = 266 ± 11 Ma
MSWD = 2.7; n = 14
(mean 207Pb corrected date : 279.9 ± 2.9)
(c) PONT-26: Equigranular leucogranite
Int. age = 272.8 ± 6.4 Ma
MSWD = 0.39; n = 14
(mean 207Pb corrected date : 279.6 ± 2.1)
(d) PONT-20: Late eq. leucogranite
Int. age = 278 ± 15 Ma
MSWD = 0.84; n = 11
(mean 207Pb corrected date : 280.9 ± 2.1)
207Pb/206Pb
238U/206Pb
5200
4400
3600
2800
2000
1200
400
U

Figure 14

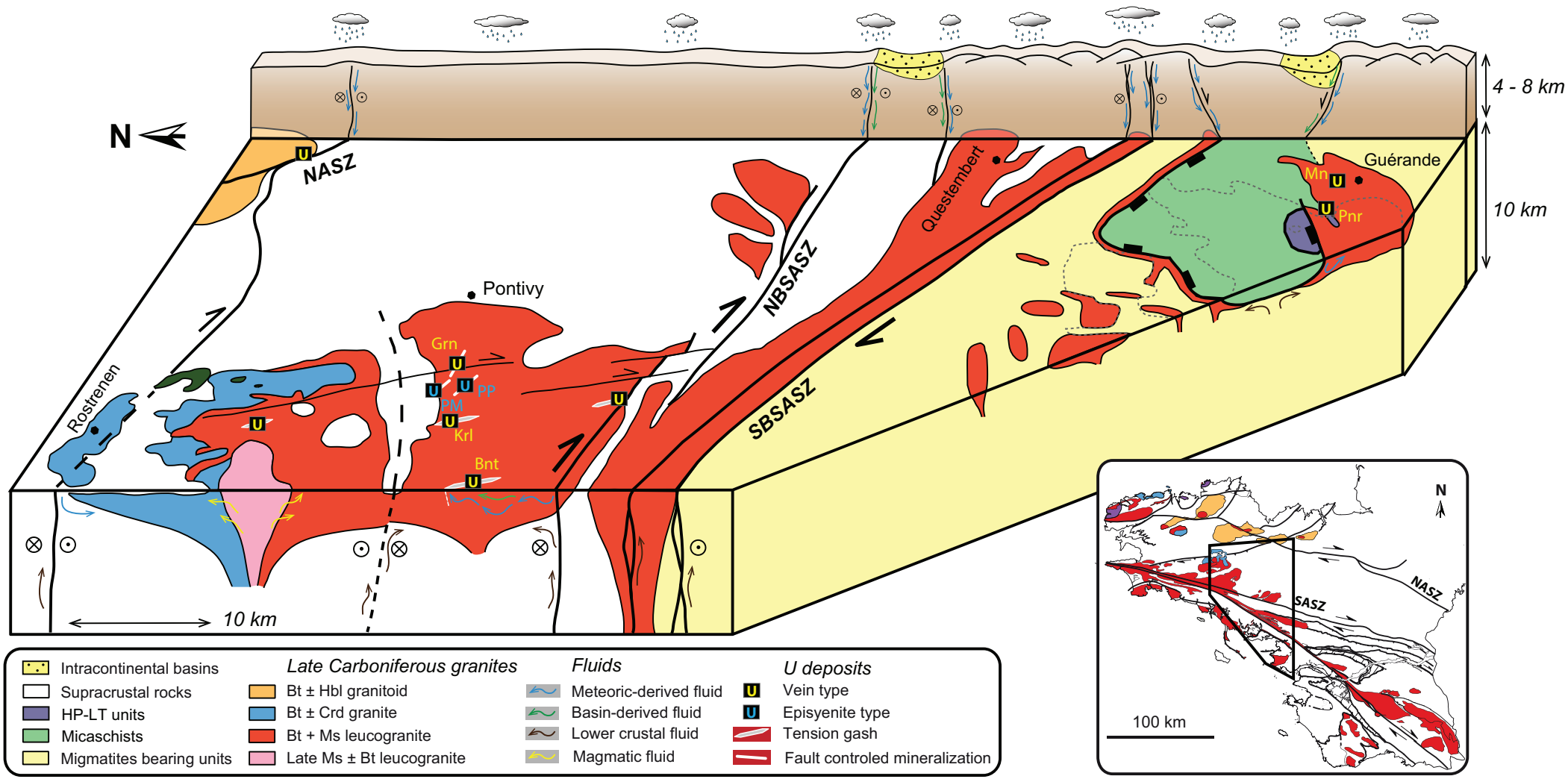
N
NASZ
Questembert
NBSASZ
SBSASZ
Pontivy
Rostrenen
Guérande
Mn
Pnr
Grn
PP
PM
Krl
Bnt
4 - 8 km
10 km
10 km
Intracontinental basins
Supracrustal rocks
HP-LT units
Micaschists
Migmatites bearing units
Late Carboniferous granites
Bt ± Hbl granitoid
Bt ± Crd granite
Bt + Ms leucogranite
Late Ms ± Bt leucogranite
Fluids
Meteoric-derived fluid
Basin-derived fluid
Lower crustal fluid
Magmatic fluid
U deposits
Vein type
Episyenite type
Tension gash
Fault controled mineralization
N
NASZ
SASZ
100 km

Table 1

Sample		MS-81-66	MS-81-32	MS-81-40
location		Prat-Mérien (PM)	Poulprio (PP)	
SiO_2	wt.%	62.97	55.95	58.24
Al_2O_3	wt.%	17.55	19.84	21.14
Fe_2O_3	wt.%	4.40	3.01	1.64
MnO	wt.%	0.04	0.03	0.03
MgO	wt.%	1.00	1.85	1.18
CaO	wt.%	1.68	1.04	0.98
Na_2O	wt.%	2.67	0.39	2.42
K_2O	wt.%	4.77	8.59	9.08
TiO_2	wt.%	0.13	0.43	0.39
P_2O_5	wt.%	1.19	0.49	0.65
LOI	wt.%	4.13	8.23	4.08
Total	wt.%	100.52	99.85	99.82
Li	ppm	91	70	66
Cs	ppm	17.2	22.8	20.2
Rb	ppm	355	544	582
Sn	ppm	4.0	15.9	15.7
W	ppm	0.89	3.02	2.47
Ba	ppm	528	645	657
Sr	ppm	53.5	46.0	56.1
Be	ppm	8.1	34.4	8.2
U	ppm	113.20	48.42	16.53
Th	ppm	0.59	18.04	14.61
Nb	ppm	2.92	12.30	7.97
Ta	ppm	0.50	2.53	1.67
Zr	ppm	41.3	178.1	157.8
Hf	ppm	1.32	5.61	4.88
Bi	ppm	2.44	0.65	0.78
Cd	ppm	0.412	0.14	0.145
Co	ppm	7.05	1.48	3.25
Cr	ppm	14.72	9.441	8.305
Cu	ppm	25.55	bdl	7.167
Ga	ppm	24.3	30.7	32.4
Ge	ppm	1.18	1.37	1.20
In	ppm	bdl	0.523	0.139
Mo	ppm	bdl	bdl	bdl
Ni	ppm	15.54	bdl	bdl
Pb	ppm	52.1	30.5	25.4
Sc	ppm	3.36	3.71	2.94
Sb	ppm	2.403	2.229	5.07
V	ppm	22.0	22.5	16.0
Y	ppm	44.34	10.91	14.10
Zn	ppm	29.43	31.29	53.36
As	ppm	95.15	20.08	54.01
La	ppm	8.13	30.40	27.24
Ce	ppm	23.90	60.93	58.68
Pr	ppm	3.94	7.47	7.18
Nd	ppm	18.02	28.40	28.45
Sm	ppm	5.77	6.85	7.61
Eu	ppm	1.11	0.83	1.12
Gd	ppm	5.89	5.42	6.31
Tb	ppm	1.14	0.68	0.83
Dy	ppm	7.79	2.92	3.59
Ho	ppm	1.65	0.41	0.50
Er	ppm	4.45	0.84	1.00
Tm	ppm	0.66	0.11	0.13
Yb	ppm	4.35	0.68	0.77
Lu	ppm	0.61	0.10	0.11
A/NK		1.84	1.99	1.53
A/CNK		1.39	1.67	1.35

LOI: Loss on ignition; bdl: below detection limit

Table 2: Average chemical composition of apatite.

Facies	Por. leucogranite		Equigranular leucogranite											
Sample	PONT-1		PONT-10						PONT-26					
Location			Core		Rim		Unzoned		Core		Rim		Unzoned	
Color CL	Yellow-green		Yellow-green		Yellow-green		Yellow-green		Yellow-green		Yellow-green		Yellow-green	
Analyses	n = 15	σ	n = 9	σ	n = 8	σ	n = 5	σ	n = 11	σ	n = 13	σ	n = 7	σ
CaO	52.42	0.71	51.97	0.44	53.17	0.55	53.16	0.91	53.21	0.39	54.19	0.73	53.95	0.45
SrO	bdl		bdl		bdl		bdl		bdl		bdl		bdl	
FeO	0.65	0.21	0.65	0.20	0.34	0.20	0.51	0.26	0.56	0.16	0.34	0.19	0.26	0.19
MnO	1.08	0.30	1.89	0.30	1.13	0.28	1.10	0.49	0.84	0.16	0.55	0.29	0.48	0.26
Na_2O	0.10	0.05	0.06	0.03	0.04	0.03	0.03	0.03	0.09	0.04	0.06	0.04	0.04	0.03
P_2O_5	41.74	0.44	41.78	0.39	41.64	0.43	41.70	0.19	41.77	0.24	41.99	0.37	42.02	0.34
SiO_2	0.01	0.01	0.02	0.01	0.01	0.01	0.02	0.02	0.01	0.02	0.02	0.02	0.03	0.02
SO_2	0.01	0.02	0.02	0.02	0.01	0.01	0.02	0.02	0.01	0.01	0.01	0.02	0.02	0.02
As_2O_3	bdl		0.01	0.01	0.01	0.01	0.01	0.02	bdl		0.01	0.01	0.01	0.01
Ce_2O_3	0.07	0.05	0.09	0.05	0.07	0.04	0.05	0.04	0.06	0.04	0.03	0.03	0.06	0.05
La_2O_3	0.03	0.03	0.02	0.02	0.01	0.01	0.02	0.04	0.01	0.02	0.02	0.02	0.02	0.02
Cl	0.012	0.007	0.003	0.003	0.008	0.006	0.008	0.003	0.004	0.003	0.005	0.005	0.002	0.003
F	3.316	0.101	3.311	0.107	3.318	0.066	3.235	0.123	3.286	0.093	3.342	0.095	3.385	0.108
Total	99.46	0.84	99.83	0.51	99.76	0.57	99.89	0.42	99.85	0.26	100.56	0.45	100.29	0.37
O=F	1.40	0.04	1.39	0.04	1.40	0.03	1.36	0.05	1.38	0.04	1.41	0.04	1.43	0.05
O=Cl	0.00	0.00	0.00	0.00	0.00	0.00	0.00	0.00	0.00	0.00	0.00	0.00	0.00	0.00
Total*	98.06	0.81	98.43	0.49	98.36	0.58	98.52	0.41	98.47	0.25	99.15	0.44	98.86	0.36
	Structural formula on the basis of a 12.5 oxygen equivalent													
Ca	4.80	0.05	4.75	0.04	4.86	0.05	4.85	0.08	4.86	0.03	4.91	0.06	4.90	0.03
Sr	0.00	0.00	0.00	0.00	0.00	0.00	0.00	0.00	0.00	0.00	0.00	0.00	0.00	0.00
Fe	0.05	0.02	0.05	0.01	0.02	0.01	0.04	0.02	0.04	0.01	0.02	0.01	0.02	0.01
Mn	0.08	0.02	0.14	0.02	0.08	0.02	0.08	0.03	0.06	0.01	0.04	0.02	0.03	0.02
Na	0.02	0.01	0.01	0.00	0.01	0.00	0.00	0.00	0.02	0.01	0.01	0.01	0.01	0.00
P	3.02	0.02	3.02	0.01	3.01	0.01	3.01	0.01	3.01	0.01	3.01	0.02	3.01	0.01
Si	0.00	0.00	0.00	0.00	0.00	0.00	0.00	0.00	0.00	0.00	0.00	0.00	0.00	0.00
S	0.00	0.00	0.00	0.00	0.00	0.00	0.00	0.00	0.00	0.00	0.00	0.00	0.00	0.00
As	0.00	0.00	0.00	0.00	0.00	0.00	0.00	0.00	0.00	0.00	0.00	0.00	0.00	0.00
Ce	0.00	0.00	0.00	0.00	0.00	0.00	0.00	0.00	0.00	0.00	0.00	0.00	0.00	0.00
La	0.00	0.00	0.00	0.00	0.00	0.00	0.00	0.00	0.00	0.00	0.00	0.00	0.00	0.00
Cl	0.00	0.00	0.00	0.00	0.00	0.00	0.00	0.00	0.00	0.00	0.00	0.00	0.00	0.00
F	0.90	0.02	0.89	0.03	0.90	0.02	0.87	0.03	0.89	0.02	0.89	0.03	0.91	0.03
OH[a]	0.10	0.02	0.11	0.03	0.10	0.02	0.13	0.03	0.11	0.02	0.11	0.03	0.09	0.03

Facies	Late eq. leucogranite		Episyenite						Monzogranite		Quartz monzodiorite			
Sample	PONT-20		MS-81-66 (PM)						PONT-22		PONT-7		PONT-23	
Location														
Color CL	Yellow-green		Blue		Red-pink		Yellow-green		Yellow-green		Purple		Purple	
Analyses	n = 17	σ	n = 11	σ	n = 4	σ	n = 4	σ	n = 23	σ	n = 14	σ	n = 15	σ
CaO	52.41	0.67	54.47	0.30	52.42	0.67	53.03	1.36	53.21	0.63	53.62	0.51	53.87	0.41
SrO	bdl		bdl		0.08	0.01	bdl		bdl		bdl		0.01	0.01
FeO	0.77	0.24	0.01	0.02	0.05	0.03	0.42	0.28	0.23	0.05	0.05	0.02	0.04	0.02
MnO	0.75	0.12	0.03	0.03	bdl		1.04	0.66	0.31	0.04	0.05	0.02	0.04	0.02
Na_2O	0.12	0.02	0.01	0.01	0.02	0.02	0.08	0.06	0.12	0.02	0.02	0.01	0.02	0.02
P_2O_5	42.61	0.29	42.79	0.38	37.15	0.43	42.64	0.37	42.04	0.50	41.63	0.40	41.59	0.59
SiO_2	0.01	0.01	0.02	0.02	0.02	0.02	0.01	0.02	0.05	0.06	0.48	0.29	0.22	0.13
SO_2	0.01	0.02	0.01	0.02	0.01	0.02	0.00	0.00	0.01	0.01	0.01	0.02	0.02	0.02
As_2O_3	bdl		0.11	0.36	5.17	0.49	0.02	0.02	bdl		0.01	0.01	bdl	
Ce_2O_3	0.09	0.05	0.03	0.04	0.08	0.04	0.04	0.03	0.03	0.03	0.24	0.15	0.19	0.12
La_2O_3	0.03	0.02	0.01	0.01	0.04	0.04	0.03	0.03	0.01	0.01	0.06	0.05	0.07	0.06
Cl	0.011	0.004	0.005	0.005	0.007	0.010	0.078	0.054	0.030	0.009	0.055	0.014	0.090	0.030
F	3.323	0.107	3.377	0.136	2.784	0.114	3.305	0.126	3.395	0.097	3.332	0.094	3.430	0.090
Total	100.14	0.59	100.89	0.37	97.85	1.01	100.68	0.77	99.45	0.71	99.57	0.59	99.58	0.68
O=F	1.40	0.05	1.42	0.06	1.17	0.05	1.39	0.05	1.43	0.04	1.40	0.04	1.44	0.04
O=Cl	0.00	0.00	0.00	0.00	0.00	0.00	0.02	0.01	0.01	0.00	0.01	0.00	0.02	0.01
Total*	98.74	0.58	99.46	0.36	96.68	1.00	99.27	0.75	98.01	0.70	98.15	0.58	98.12	0.65
	Structural formula on the basis of a 12.5 oxygen equivalent													
Ca	4.75	0.05	4.89	0.02	5.02	0.02	4.78	0.08	4.86	0.05	4.89	0.06	4.93	0.03
Sr	0.00	0.00	0.00	0.00	0.00	0.00	0.00	0.00	0.00	0.00	0.00	0.00	0.00	0.00
Fe	0.05	0.02	0.00	0.00	0.00	0.00	0.03	0.02	0.02	0.00	0.00	0.00	0.00	0.00
Mn	0.05	0.01	0.00	0.00	0.00	0.00	0.07	0.05	0.02	0.00	0.00	0.00	0.00	0.00
Na	0.02	0.00	0.00	0.00	0.00	0.00	0.01	0.01	0.02	0.00	0.00	0.00	0.00	0.00
P	3.05	0.01	3.04	0.02	2.81	0.02	3.04	0.01	3.03	0.02	3.00	0.02	3.00	0.02
Si	0.00	0.00	0.00	0.00	0.00	0.00	0.00	0.00	0.00	0.01	0.04	0.02	0.02	0.01
S	0.00	0.00	0.00	0.00	0.00	0.00	0.00	0.00	0.00	0.00	0.00	0.00	0.00	0.00
As	0.00	0.00	0.01	0.02	0.28	0.03	0.00	0.00	0.00	0.00	0.00	0.00	0.00	0.00
Ce	0.00	0.00	0.00	0.00	0.00	0.00	0.00	0.00	0.00	0.00	0.01	0.00	0.01	0.00
La	0.00	0.00	0.00	0.00	0.00	0.00	0.00	0.00	0.00	0.00	0.00	0.00	0.00	0.00
Cl	0.00	0.00	0.00	0.00	0.00	0.00	0.01	0.01	0.00	0.00	0.01	0.00	0.01	0.00
F	0.89	0.03	0.90	0.03	0.79	0.03	0.88	0.03	0.91	0.03	0.90	0.03	0.93	0.02
OH[a]	0.11	0.03	0.10	0.03	0.21	0.03	0.11	0.03	0.08	0.03	0.09	0.03	0.06	0.02

Notes: oxide in wt.%, cationic contents in apfu. [a]: calculated OH cationic content. bdl: below detection limit; Por. Leucogranite: porphyritic leucogranite; Late eq. leucogranite: late equigranular leucogranite.

Table 3

Sample	***Emplacement age (U-Pb zircon)***	***Unforced discordia dates***	***Age used for common Pb***	***^{207}Pb corrected dates***
Porphyritic leucogranite (PONT-1)	316.7 ± 2.5 Ma *(MSWD = 1.2)*	285.4 ± 8.5 Ma *(MSWD=6.8)*	285 Ma	307.2 ± 7.1 Ma **286.2 ± 3.8 Ma**
Equigranular leucogranite (PONT-10)	310.3 ± 4.7 Ma *(MSWD = 2.5)*	270.4 ± 6.7 Ma *(MSWD=2.5)*	270 Ma	294.9 ± 7.4 Ma **279.9 ± 2.9 Ma**
Equigranular leucogranite (PONT-26)		272.8 ± 2.9 Ma *(MSWD = 1.2)*	275 Ma	299.9 ± 4.3 Ma **279.6 ± 2.1 Ma**
Late eq. leucogranite (PONT-20)	304.7 ± 2.7 Ma *(MSWD = 0.57)*	278 ± 11 Ma *(MSWD = 8.7)*	280 Ma	297.1 ± 3 Ma **280.9 ± 2.1 Ma**
Episyenite (MS-81-66-PM)		289 ± 10 Ma *(MSWD = 0.54)*	290	**286.5 ± 3.8 Ma**
Monzogranite (PONT-22)	315.5 ± 2.0 Ma *(MSWD = 1.5)*	317.8 ± 4.9 Ma *(MSWD = 1.2)*	315	**320.6 ± 3.1 Ma**
Monzodiorite Quartzique (PONT-7)	315.2 ± 2.9 Ma *(MSWD = 0.94)*	298 ± 13 Ma *(MSWD = 1.17)*	315	**310.4 ± 7.5 Ma**

Note: Late eq. leucogranite: late equigranular leucogranite